The Astrophysical Journal, 631:838–855, 2005 October 1

EQUILIBRIUM DISK-BULGE-HALO MODELS FOR THE MILKY WAY AND ANDROMEDA GALAXIES

Lawrence M. Widrow
Department of Physics, Queen's University, Kingston, ON K7L 3N6, Canada; widrow@astro.queensu.ca

and

John Dubinski
Department of Astronomy and Astrophysics, University of Toronto, 60 St. George Street,
Toronto, ON M5S 3H8, Canada; dubinski@astro.utoronto.ca
Received 2005 January 27; accepted 2005 June 11

ABSTRACT

We describe a new set of self-consistent, equilibrium disk galaxy models that incorporate an exponential disk, a Hernquist model bulge, an NFW halo, and a central supermassive black hole. The models are derived from explicit distribution functions for each component, and the large number of parameters permit detailed modeling of actual galaxies. We present techniques that use structural and kinematic data such as radial surface brightness profiles, rotation curves, and bulge velocity dispersion profiles to find the best-fit models for the Milky Way and M31. Through *N*-body realizations of these models we explore their stability against the formation of bars. The models permit the study of a wide range of dynamical phenomenon with a high degree of realism.

Subject headings: dark matter — galaxies: individual (M31) — galaxies: structure — Galaxy: general — methods: *n*-body simulations

1. INTRODUCTION

The modeling of spiral galaxies to match photometric and dynamical measurements is a time-honored endeavor. A complete and accurate characterization of the structural and kinematical properties of galaxies is necessary to understand the diversity of galactic dynamical behavior and the origin of galaxies in the current cosmological paradigm.

This paper presents a new set of models for the phase-space distribution functions (DFs) of axisymmetric disk galaxies. The models consist of an exponential disk, a Hernquist model bulge (Hernquist 1990), an NFW halo (Navarro et al. 1996), and a central, supermassive black hole. They are defined by a large number of parameters that permit detailed modeling of real galaxies by fitting to observational constraints. Although the models represent self-consistent equilibrium solutions to the coupled Poisson and collisionless Boltzmann (CB) equations, they are subject to both local and global nonaxisymmetric instabilities and are therefore suitable as initial conditions for numerical studies of galactic dynamics.

The standard practice in modeling disk galaxies has been to assume simple functional forms for the space density and gravitational potential of the disk, bulge, and halo and then fit to a wide range of observational data. For the Milky Way galaxy, optimal structural parameters for these "mass models" are found primarily from surface brightness photometry, local stellar kinematics, the circular rotation curve, and observations of dynamical tracer populations such as globular clusters, the Magellanic clouds, and the dwarf satellite galaxies. These observational constraints have been used to determine the best-fit model parameters based on χ^2 minimization techniques (see, e.g., Innanen 1973; Clutton-Brock et al. 1977; Bahcall & Soneira 1980; Caldwell & Ostriker 1981; Kuijken & Gilmore 1991; Rohlfs & Kreitschmann 1988; Malhotra 1995; Kochanek 1996; Dehnen & Binney 1998a; Wilkinson & Evans 1999; Klypin et al. 2002).

For external galaxies, the problem is somewhat simpler because of the advantage of an outside view and the smaller number of observational constraints. Optical and infrared deprojected surface brightness profiles of the stellar distribution are combined with rotation curves measured from H I gas kinematics to build mass models. The standard method is to perform a bulge-disk decomposition of the surface brightness profile usually into an $R^{1/4}$ law surface density profile for the bulge and a radial exponential profile for the disk (see, e.g., Kent 1985; Simien & de Vaucouleurs 1986; Binney & Merrifield 1998; see also Courteau et al. 1996 and references therein for a discussion of bulge-disk decomposition with the more general Sérsic law for the bulge). The halo model parameters are inferred by fitting multicomponent mass models to the rotation curve data assuming values for the mass-to-light ratios of the disk and bulge stars. For nearby galaxies such as M31, kinematic data for the globular cluster, planetary nebulae, and satellite systems are used to refine the models (Evans & Wilkinson 2000).

There has also been parallel work in developing realistic *N*-body realizations of galaxy models for numerical experimentation in disk stability and galaxy interactions and mergers. To generate an *N*-body realization, it is necessary to model the full DFs for the multicomponent system, in principle by solving the coupled Poisson and CB equations. Owing to the complexity of these equations, various approximation schemes have been used. Early work on disk galaxy simulations set up initial conditions by estimating the velocity dispersion for a stable disk model with Toomre parameter $Q > 1$ and then assuming a locally Gaussian distribution for the velocities (see, e.g., Sellwood 1985). Barnes (1988) built three-component models by adiabatically growing a disk potential within a live halo model and then adding an *N*-body disk with initial conditions generated as above. Hernquist (1993) presented a simpler approximate prescription for three-component disk-bulge-halo models where the bulge and halo velocity distributions are assumed to be Maxwellian, truncated at the local escape speed and with dispersions estimated from the Jeans equations. These methods, while convenient, produce models that are slightly out of equilibrium and so require some relaxation time to damp out transients. Moreover, the models readjust to a state different from the one proposed (see, e.g., Kazantzidis et al. 2004).

As numerical methods and resolution improve, it has become necessary to develop more sophisticated techniques to generate initial conditions. Toward this end, Kuijken & Dubinski (1995, hereafter KD95) presented a set of semianalytic models for the DFs of disk galaxies consisting of an exponential disk, a centrally concentrated bulge, and an extended halo. The DFs are constructed from integrals of motion and use an iterative scheme to generate self-consistent solutions to the Poisson and CB equations. They have been used extensively to study different aspects of galaxy internal dynamics and interactions (e.g., Dubinski & Kuijken 1995; Dubinski 1998; Dubinski et al. 1999; Garcia-Ruiz et al. 2002; O'Neill & Dubinski 2003; Widrow et al. 2003). An iterative scheme of this sort has been used by other authors including Debattista & Sellwood (1998, 2000) in their work on the evolution of bars.

Fitting models to actual galaxies requires one to "observe" the model and compare with real observations. By providing the full DFs, the KD95 models enable one to add a level of realism to these pseudo-observations that is not possible with simple mass models. For example, a mass model rotation curve is constructed directly from the potential rather than from model line-of-sight velocities. With the KD95 models it is possible to construct the stellar rotation curve directly from stellar velocities and thereby incorporate asymmetric drift. Gravitational microlensing experiments provide another example where improved pseudo-observations are possible since the full DF allows for a self-consistent calculation of the predicted event rate distribution (Widrow et al. 2003).

The bulge and halo of the KD95 models are characterized by a constant-density core. Since their development it has become widely accepted from numerous cosmological simulations that dark halos have cuspy centers (Dubinski & Carlberg 1991; Navarro et al. 1996). Detailed analysis of the central surface brightness and velocity dispersion profiles of early-type galaxies and bulges suggest that these systems are also cuspy at their centers and furthermore contain supermassive black holes. We are therefore motivated to develop a new set of axisymmetric disk galaxy models with cuspy halos and bulges that also allow for the self-consistent addition of a supermassive central object. These models have many purposes. They provide the gravitational potential and mass and velocity distributions from the sphere of influence of the central black hole in the inner few parsecs out to the virial radius of the model galaxy. Circular velocity curves, rotation curves incorporating asymmetric drift, velocity ellipsoids, line-of-sight velocity distributions (LOSVDs), and surface density (brightness) profiles can be generated easily. The large parameter space permits a wide range of models for comparison to real galaxies, and the good quality of the initial equilibria makes them ideal for studying subtle dynamical processes such as bar formation and disk warping and heating.

The DFs are described in § 2. Examples that match photometric and dynamical data for the Milky Way and M31 are presented in § 3. This section also presents results from numerical experiments on the stability of these models, as well as a brief discussion of an M31 model that incorporates a supermassive black hole. We conclude in § 4 with a summary and a discussion of possible applications of the models.

2. DISTRIBUTION FUNCTIONS

The phase-space DFs for the disk, bulge, and halo of the KD95 models are chosen analytic functions of the integrals of motion. By Jeans theorem, any such DF yields a steady state solution of the CB equation in any potential that respects these integrals (Binney & Tremaine 1987). A self-consistent self-gravitating model is one in which the potential and space density also satisfy the Poisson equation.

The KD95 models are, by design, axisymmetric with two known integrals of motion, the energy E and the angular momentum about the symmetry axis J_z. KD95 choose the King model DF for the bulge, which, in isolation, yields a system that is spherically symmetric and has a density profile characterized by a constant-density core, an r^{-2} falloff at intermediate radii, and a finite "tidal" radius where the density vanishes. For the halo, KD95 use the DF of a lowered Evans model, which also exhibits a constant-density core, power-law intermediate region, and tidal radius. (We denote the tidal radius of the halo, which represents the outer edge of the system as a whole, as r_t.)

The configuration and velocity space distributions of the King and lowered Evans models are modified once they are incorporated into a multicomponent model. Recall that for a system of collisionless particles in a static potential, any $f(E)$ (i.e., any DF that is a function only of the energy) yields a steady state solution of the CB equation whose velocity distribution is isotropic (Binney & Tremaine 1987). For an isolated self-gravitating system, ρ and Ψ are necessarily spherically symmetric (for a proof see Perez & Aly 1996). In the presence of an aspherical external potential, an $f(E)$ will yield an aspherical mass distribution through the dependence of E on Ψ. However, the velocities remain isotropic so long as f does not depend on angular momentum or some other integral of motion. For the multicomponent models considered here and in KD95, the disk potential causes a slight flattening of the bulge and halo.

In this section we describe new models that have an NFW halo, a Hernquist bulge, and a central supermassive black hole. We begin by presenting DFs for the bulge and halo taken in isolation and then describe how these DFs are modified for composite models.

2.1. *The Halo Distribution Function*

Navarro et al. (1996) found that the density profiles of dark matter halos in their cosmological simulations have a "universal" shape (the so-called NFW profile) of the form

$$\rho_{\rm NFW}(r) = \frac{\rho_h}{(r/a_h)(1 + r/a_h)^2}, \tag{1}$$

where a_h is the scale radius, $\rho_h \equiv \sigma_h^2/4\pi a_h^2$ is a characteristic density, and σ_h is a characteristic velocity dispersion. (Here and throughout we set Newton's constant $G = 1$.) In contrast with the profile of the Evans model halo, $\rho_{\rm NFW}$ has an inner r^{-1} cusp and an extended r^{-3} outer halo. The gravitation potential for this profile is

$$\Phi_{\rm NFW}(r) = -\sigma_h^2 \frac{\log(1 + r/a_h)}{r/a_h}. \tag{2}$$

Our strategy is to use a DF that, in the absence of a disk or bulge, yields a spherically symmetric NFW halo. We assume that the velocity dispersion is isotropic so that the DF depends only on the energy E. (Formally, E is the energy per unit mass.) For a given density profile, the DF can then be calculated through an Abel transform (Binney & Tremaine 1987), a procedure that has been carried out for the NFW profile by Zhao (1997), Widrow (2000), and Lokas & Mamon (2001). We write the DF as a function of the relative energy $\mathcal{E} \equiv -E$,

$$f_{\rm NFW}(\mathcal{E}) = \sigma_h^{-1} a^{-2} \mathcal{F}_{\rm NFW}\left(\mathcal{E}/\sigma_h^2\right). \tag{3}$$

For the dimensionless DF $\mathcal{F}$ we use the analytic fitting formula

$$\mathcal{F}_{\rm NFW}(\epsilon) = \begin{cases} \dfrac{3}{2^{9/2}\pi^2}\epsilon^{3/2}(1-\epsilon)^{-5/2}\left(\dfrac{-\log\epsilon}{1-\epsilon}\right)^{\alpha} e^{P}, & 0<\epsilon<1, \\ 0 & \text{otherwise}, \end{cases} \tag{4}$$

where $P = P(\mathcal{E})$ is a fourth-order polynomial with $P(1) = 0$ and $\alpha = 2.71$ (Widrow 2000).

The NFW profile is infinite in extent and mass. For model building it is desirable to have a finite halo and so, following King (1966), we introduce an energy cutoff $E_h \equiv -\mathcal{E}_h \equiv -\epsilon_h\sigma_h^2$ and replace $f_{\rm NFW}$ with

$$f_{\rm halo}(\mathcal{E}) = \sigma_h^{-1}a_h^{-2}\mathcal{F}_{\rm halo}\left(\mathcal{E}/\sigma_h^2\right), \tag{5}$$

where

$$\mathcal{F}_{\rm halo}(\epsilon) = \begin{cases} \mathcal{F}_{\rm NFW}(\epsilon) - \mathcal{F}_{\rm NFW}(\epsilon_h), & \epsilon_h<\epsilon<1, \\ 0, & \text{otherwise}, \end{cases} \tag{6}$$

setting $\epsilon_h = 0$ yields a full NFW profile while $0 < \epsilon_h < 1$ yields a truncated profile. Examples with $a_h = \sigma_h = 1$ and various values of ϵ_h are shown in Figure 1. Note that the truncation radius can be varied independently of the characteristic density and scale radius. When building models a natural choice for the truncation radius is the cosmologically motivated virial radius, $r_{\rm vir}$ (see below). After the inner properties of a model galaxy are set, a value of ϵ_h that gives $r_t \approx r_{\rm vir}$ can be easily found. In contrast, for the King and lowered Evans models a change in the truncation radius results in a significant change in the inner profile, making model building more cumbersome and less intuitive.

The DF as written above is symmetric under $J_z \rightarrow -J_z$ and therefore generates a model with no net rotation. By splitting the DF into parts with positive and negative J_z ($\mathcal{F}_{\pm}$) and recombining them with a suitable coefficient, one can generate a model with arbitrary amounts of rotation. Formally we write

$$\mathcal{F}_{\rm halo} = \alpha_h\mathcal{F}_{+} + (1-\alpha_h)\mathcal{F}_{-}, \tag{7}$$

where α_h controls the amount of rotation ($\alpha_h = \frac{1}{2}$ implies no rotation).

2.2. *The Bulge Distribution Function*

Bulges are commonly modeled as the de Vaucouleurs $r^{1/4}$ law (de Vaucouleurs 1948) in projection, and the Hernquist model is a simple density-potential pair that closely mimics this behavior (Hernquist 1990). We therefore model the bulge using a Hernquist DF modified by an energy cutoff E_b to truncate the profile in a fashion similar to what was done for the halo.

The standard Hernquist model has a density profile and potential given by

$$\rho_{\rm H} = \frac{\rho_b}{(r/a_b)(1+r/a_b)^3} \tag{8}$$

and

$$\Phi_{\rm H} = -\frac{\sigma_b^2}{1+r/a_b}, \tag{9}$$

where a_b, $\rho_b = \sigma_b^2/2\pi a_b^2$, and σ_b are the scale length, characteristic density, and characteristic velocity of the bulge, respectively. While the total mass is finite, the density distribution is infinite in extent with $\rho \propto r^{-4}$ at large radii.

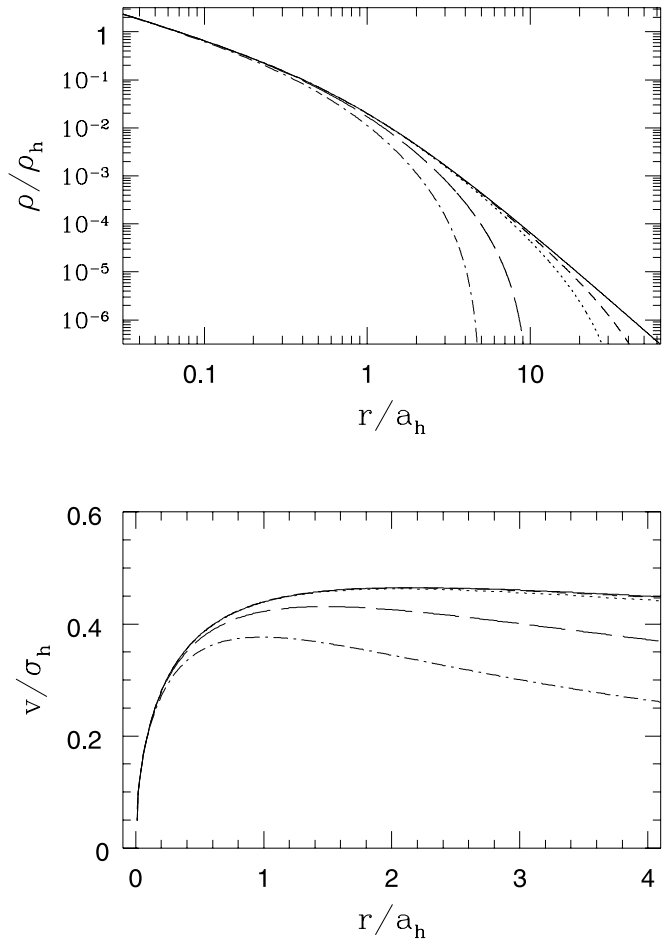

FIG. 1.—Density profiles (*top*) and rotation curves (*bottom*) for halo models with $a_h = \sigma_h = 1$ and values of $\mathcal{E}_h$ corresponding to tidal radii $r_t = 5$, 10, 40, and 80. Also shown is the full NFW model (*solid line*).

We modify the Hernquist DF by incorporating an energy cutoff:

$$f_{\rm bulge}(\mathcal{E}) = \sigma_b^{-1}a_b^{-2}\mathcal{F}_{\rm bulge}\left(\mathcal{E}^{1/2}/\sigma_b\right), \tag{10}$$

where

$$\mathcal{F}_{\rm bulge}(q) = \begin{cases} \mathcal{F}_{\rm H}(q) - \mathcal{F}_{\rm H}(q_b), & q_b<q<1, \\ 0, & \text{otherwise}, \end{cases} \tag{11}$$

$q_b \equiv (-E_b/\sigma_b^2)^{1/2}$, and $\mathcal{F}_{\rm H}$ is the infinite-extent Hernquist model DF,

$$\mathcal{F}_{\rm H}(q) = \frac{1}{2^{7/2}\pi^3}\frac{1}{(1-q^2)^{5/2}} \times\left[3\sin^{-1}q + q\left(1-q^2\right)^{1/2}\left(1-2q^2\right)\left(8q^4-8q^2-3\right)\right]. \tag{12}$$

As with the halo, rotation is introduced through an additional parameter α_b.

It is straightforward to use other models for the bulge. For example, the potential and DF for the density profile $\rho \propto r^{-3/2}(r+a)^{-5/2}$ are analytic, and the associated surface density profile provides a somewhat better match to the de Vaucouleurs law than the surface density profile of the Hernquist model (Dehnen 1993).

2.3. *The Disk Distribution Function*

The disk is assumed to be axisymmetric with space density $\rho_{\rm disk} = \rho_{\rm disk}(R,\ z)$ and quasi-Maxwellian DF taken directly from the KD95 models, which, in turn, were based on the two-dimensional model by Shu (1969) and extensions by Binney (1987). This DF is a function of E, J_z, and E_z, the latter being an approximate third integral of motion that corresponds to the energy in vertical oscillations. An implicit assumption in the formulation of this DF is that the velocity dispersions are small so that the epicyclic approximation is valid in the treatment of disk star orbits. This assumption limits the application of the models to cool disks. The DF can be tuned to yield a space density of a desired form. As in KD95, we assume that the surface density profile of the disk is exponential in the radial direction with scale radius R_d and truncation radius $R_{\rm out}$. The vertical structure is given approximately by $\mathrm{sech}^2\,(z/z_d)$, where z_d is the vertical scale height. In all, five parameters define the space density of the disk: R_d, $R_{\rm out}$, z_d, the mass M_d, and a profile "shape" parameter $\delta R_{\rm out}$, which governs the sharpness of the truncation.

The "stars" of the KD95 disks have nonzero velocity dispersions in the radial, azimuthal, and vertical directions. The dispersion in the radial direction, $\sigma_R(R)$, is assumed to be exponential: $\sigma_R^2(R) = \sigma_{R0}^2 \exp\,(-R/R_\sigma)$. For simplicity, we set $R_\sigma = R_d$ in accord with observations by Bottema (1993). The dispersion in the azimuthal direction is related to σ_R through the epicycle equations (Binney & Tremaine 1987), while the dispersion in the vertical direction is set by the vertical potential gradient and the vertical scale height.

In total, the DFs for the three components are characterized by 15 parameters, which we collect for convenience in Table 1.

2.4. *DFs for the Composite Model*

An isolated model halo is constructed by solving Poisson's equation self-consistently for the gravitational potential

$$\nabla^2\Phi_{\rm halo} = 4\pi\rho_{\rm halo} \tag{13}$$

together with the integral relation between the DF (eq. [6]), the density, and the relative potential $\psi \equiv -\Phi$:

$$\rho_{\rm halo} = 2^{5/2}\pi \int_0^\psi d\mathcal{E}\sqrt{(\mathcal{E}-\psi)}f_{\rm halo}(\mathcal{E}) \tag{14}$$

(Binney & Tremaine 1987). For a disk-bulge-halo model, equation (13) is replaced by

$$\nabla^2\Phi = 4\pi\rho, \tag{15}$$

where

$$\rho = \int d^3v\,\left(f_{\rm disk} + f_{\rm bulge} + f_{\rm halo}\right) \tag{16}$$

is the total density.

The DFs in this expression depend on the energy (as well as other integrals of motion), which in turn depends on Φ. Since Φ is the total gravitational potential, the density fields of the different components are interrelated in a complicated way. In fact, the components of a disk-bulge-halo model constructed from equation (6) of KD95 and equations (6) and (10) may bare little resemblance to the corresponding isolated components, a situation that is cumbersome for model building.

TABLE 1

Summary of Model Parameters

Parameter	Description
ϵ_h	Halo tidal radius parameter
σ_h	Halo characteristic velocity
a_h	Halo scale length
α_h	Halo rotation parameter
M_d	Disk mass
R_d	Disk scale length
$R_{\rm out}$	Disk truncation radius
$\delta R_{\rm out}$	Sharpness of truncation
h_d	Disk scale height
σ_{R0}	Radial velocity dispersion at galaxy center
R_σ	Scale length for radial dispersion
ϵ_b	Bulge tidal radius parameter
σ_b	Characteristic bulge velocity
a_b	Bulge scale length
α_b	Bulge rotation parameter

To alleviate this problem, we proceed as follows. The DF for an isolated halo is nonzero over the energy range $\mathcal{E}\in\{\mathcal{E}_h,\ \sigma_h^2\}$. Qualitatively, we may expect the energy range of halo particles in the multicomponent system to be extended to $\mathcal{E}\in\{\mathcal{E}_h,\ \sigma_h^2 + \sigma_b^2 + \sigma_d^2\}$, where $\sigma_d^2 \equiv M_d/R_d$ is the depth of the disk potential. These arguments suggest that we replace $f_{\rm halo}(\mathcal{E})$ of equation (5) by $f_{\rm halo}\left(\mathcal{E}_h'(\mathcal{E})\right)$, where $\mathcal{E}_h'(\mathcal{E})$ is a function that maps the energy of a particle in the composite system ($\mathcal{E}$) to the energy of a particle in the would be isolated halo ($\mathcal{E}_h'$). In what follows, we assume

$$\mathcal{E} = \mathcal{E}_h'\left(1 + \frac{\sigma_b^2 + \sigma_d^2}{\sigma_h^4}\mathcal{E}_h'\right). \tag{17}$$

By construction, at low binding energies ($\mathcal{E} \to 0$), $\mathcal{E}_h' \simeq \mathcal{E}$ whereas $\mathcal{E} \to \sigma_h^2 + \sigma_b^2 + \sigma_d^2$ as $\mathcal{E}_h' \to \sigma_h^2$. For the bulge, we replace $f_{\rm bulge}(\mathcal{E})$ with $f_{\rm bulge}\left(\mathcal{E}_b'(\mathcal{E})\right)$, with $\mathcal{E}_b(\mathcal{E}) = \mathcal{E}_b' + \sigma_h^2 + \sigma_d^2$.

These mappings are by no means unique and, apart from the conditions discussed above, are not motivated by any particular physical model. Indeed, other mappings can be shown to yield similar and equally acceptable models.

In Figure 2 we show an example of the density profile and rotation curve for a typical disk-bulge-halo model. (The model parameters are given in Table 2.) Also shown is the halo profile that results assuming the same values of the a_h, σ_h^2, and $\mathcal{E}_h$ if the disk and bulge are not included.

2.5. *Comment on Adiabatic Compression*

It is important to stress that the "isolated halo" in Figure 2 is not meant to represent the progenitor for the halo in the final composite model. Indeed, the structure of dark halos in fully developed disk galaxies can be determined only through detailed modeling of galaxy formation. According to the standard structure formation paradigm, at early times baryons and dark matter are well mixed. Disks form when the (collisional) baryons lose energy (but not angular momentum) and settle to the bottom of the dark halo potential well. The halo in turn responds to the change in the gravitational potential and therefore a pristine NFW halo will readjust to a new configuration.

Simulations of galaxy formation that include gas dynamics and star formation are still relatively crude and computationally expensive. An alternative is to treat the effect of baryon infall on dark halos as an adiabatic process (Blumenthal et al. 1986; Flores et al. 1993). If changes in the potential are slow compared with the orbital time of dark halo particles, then for each

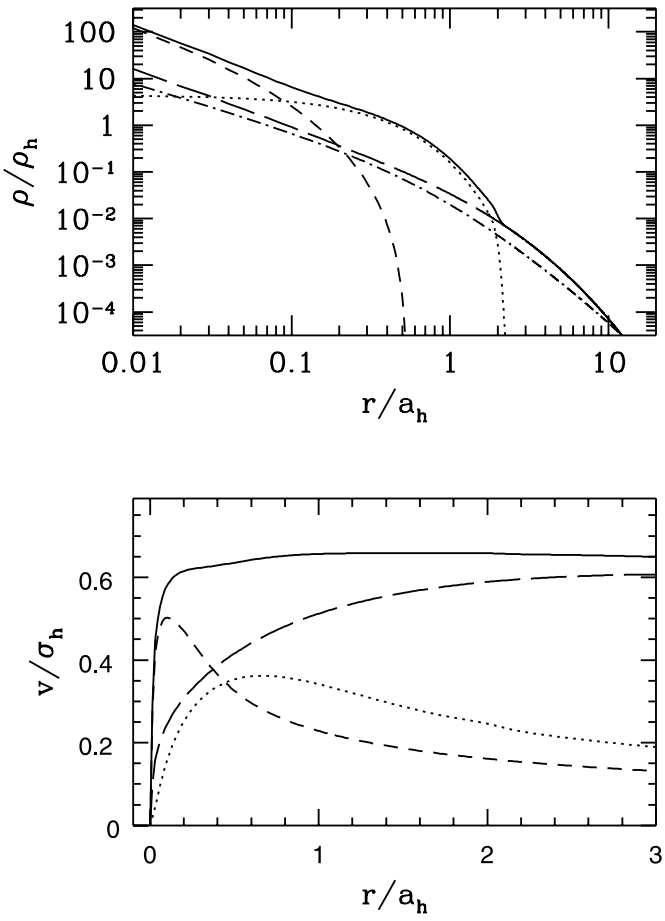

FIG. 2.—Density profile (*top*) and rotation curve (*bottom*) for the disk-bulge-halo model described in the text. Shown are the contributions from the disk (*dotted line*), bulge (*dashed line*), halo (*long-dashed line*), as well as the total density profile and rotation curve (*solid line*). Also shown is the halo model that results if the same halo parameters are used and the disk and bulge are not included (*dot-dashed line in the top panel*).

particle, there is a set of quantities known as adiabatic invariants that remain approximately constant even as the orbit changes. Knowledge of the adiabatic invariants allows one to determine the final DF from the initial DF without having to model the evolution of the system explicitly.

Under a rather restrictive set of assumptions, the adiabatic theorem leads to the following simple relation:

$$\left[M_{\rm baryon}(r) + M_{\rm dm}\right] r = M_{\rm halo}(r_i) r_i \qquad (18)$$

(Young 1980; Blumenthal et al. 1986; Flores et al. 1993). In this formula, $M_{\rm baryon}(r)$ is the baryon mass distribution as a function of radius (i.e., a spherically averaged representation of the disk and bulge), $M_{\rm dm}$ is the final distribution of the dark halo, and $M_{\rm halo}(r_i)$ is the initial distribution of the baryon–dark matter protogalaxy. Equation (18) allows one to go directly from the cosmologically motivated NFW halo to the final dark halo in a fully formed galaxy and has been used extensively in modeling disk galaxies (see, e.g., Mo et al. 1998; Klypin et al. 2002).

In general, the dark halos predicted by equation (18) are more centrally concentrated than the progenitors with a density profile that is cuspier in the center (e.g., the r^{-1} cusp becomes an $r^{-1.5}$ cusp as in Fig. 7 of Klypin et al. 2002). However, equation (18) is based on a number of suspect assumptions. In addition to spherical symmetry and adiabaticity, one must assume that the dark halo particles are on circular orbits and therefore do not cross as their orbits contract. The particle orbits in simulated halos are, if anything, radially biased (see Moore et al. [2004], who study the importance of the distribution of orbits for the evolution of dark halos).

An indication of the uncertainty in the adiabatic prescription can be seen in Figure 7 of Klypin et al. (2002), where two halos from the same progenitor are shown. In one case, equation (18) is used to determine the halo profile, while in the other, baryons and dark matter are allowed to exchange angular momentum. The difference between the two halos is significant, with the former being denser in the central regions by a factor of 30!

How do our models fit in with the adiabatic compression paradigm? In short, we sidestep the issue by focusing on models of fully developed disk galaxies. One might use equation (18) to work backward from our final model and determine the progenitor (and thus compare with the NFW profile), but given the caveats associated with this equation, we do not see this as a particularly fruitful endeavor. We do note that the difference between a model halo in isolation and one incorporated into a composite system is consistent with the general predictions of adiabatic compression theory (the profile exhibits a slightly cuspier inner region and is generally more concentrated) and so the naive use of the halo parameters as an indication of the general structure of the progenitor halo seems a reasonable first pass for making contact with cosmology.

2.6. *Models with Central Supermassive Black Holes*

The observation that most, if not all, disk galaxies harbor supermassive black holes near their centers has led to considerable interest in the structure of black hole–stellar systems, as well as the effect a black hole might have on the central cusp of a dark matter halo. Tremaine et al. (1994) have derived DFs for a variety of models with central black holes whose density profiles have $r^{-\eta}$ central cusps and r^{-4} outer parts. These so-called η-models include the Hernquist profile ($\eta = 1$) and are therefore directly applicable to the bulge DF in our system and easily generalized to the NFW halo model. The DFs of Tremaine et al. (1994) produce a density profile that is independent of the black

TABLE 2
PARAMETERS FOR MODELS DISCUSSED IN THE TEXT

Model	ϵ_h	σ_h	a_h	M_d	R_d	h_d	ϵ_b	σ_b	a_b	σ_{R0}/ω_b	$(M/L_R)_d$	$(M/L_R)_b$
Sample.....	0.079	1	1	0.1	0.3	0.02	0.1	1.15	0.15	...	...	...
MWa.....	0.17	2.496	12.96	19.66	2.806	0.409	0.213	4.444	0.788	1.211	...	...
MWb.....	0.11	3.447	8.818	14.47	2.817	0.439	0.209	4.357	0.884	1.244	...	...
M31a.....	0.25	3.371	12.94	33.40	5.577	0.3	0.071	4.607	1.826	0.763	3.4	1.9
M31b.....	0.25	3.224	14.03	35.08	5.401	0.3	0.075	4.811	1.857	0.751	3.4	3.4
M31d.....	0.36	3.243	17.46	50.10	5.566	0.3	0.074	4.685	1.802	0.732	5.0	2.5

NOTES.—We assume $G = 1$. Units for the Milky Way and M31 models are kpc, 100 km s^{-1}, and 2.33×10^9 $M_\odot$.

hole mass: for a given η-model, the black hole alters the velocity distribution but not the space distribution of the stars and dark matter particles in its vicinity. We build black holes into our models under the same assumption.

Consider first the bulge–black hole system. The effect of a black hole of mass $M_{\rm BH}$ is to modify the relative potential

$$\psi^*(r) = \psi(r) + \frac{M_{\rm BH}}{r}, \tag{19}$$

where, as in Tremaine et al. (1994), the asterisk denotes properties of models that include a black hole. While the Hernquist DF is nonzero over the energy range $\mathcal{E} \in \{\mathcal{E}_b,\ \sigma_b^2\}$, with a black hole, the energy range is extended to $\mathcal{E}^* \in \{\mathcal{E}_b,\ \infty\}$.

In principle, disk-bulge-halo models with a central black hole can be constructed by replacing $f_{\rm bulge}$ with a DF from Tremaine et al. (1994) that is modified by a suitable energy cutoff. The DFs for the disk and halo would be similarly replaced. However, the DFs in Tremaine et al. (1994) are not analytic and would have to be recalculated for each choice of $M_{\rm BH}$. We therefore choose the following more efficient, albeit ad hoc scheme: The potential and density profile for a particular disk-bulge-halo model are calculated assuming no black hole. To incorporate a black hole, the potential is modified according to equation (19) and a new DF is found that interpolates between $f_{\rm bulge}$ of equation (10) and the DF of the appropriate η-model.

At large binding energies ($\mathcal{E}^* \to \infty$) the Hernquist–black hole DF has the asymptotic form (Tremaine et al. 1994) $\lim_{\mathcal{E}^* \to \infty} f^* = f^*_\infty$, where

$$f^*_\infty(\mathcal{E}^*) = \frac{\sigma_b}{2^{5/2}\pi^3 M_{\rm BH} a_b} \left(\frac{\mathcal{E}^*}{\sigma_b^2}\right)^{-1/2}. \tag{20}$$

On the other hand,

$$f_{\rm H}(\mathcal{E}) \to \frac{3}{2^{5/2}\pi^2 \sigma_b a_b^2} \left(1 - \mathcal{E}/\sigma_b^2\right)^{-5/2} \tag{21}$$

for $\mathcal{E} \to \sigma_b^2$. From the asymptotic form of the Hernquist potential, $\psi_{\rm H} \simeq \sigma_b^2/(1 - r/a_b)$, we have $r \simeq a_b\left(1 + \psi_{\rm H}/\sigma_b^2\right)$, suggesting

$$\mathcal{E}^* = \mathcal{E} + \frac{M_{\rm BH}}{a_b}\left(\frac{1}{1 - \mathcal{E}/\sigma_b^2} - \frac{1}{1 - \mathcal{E}_b/\sigma_b^2}\right) \tag{22}$$

as a mapping from $\mathcal{E}$ to $\mathcal{E}^*$. By construction, $\mathcal{E}^*(\mathcal{E}_b) = \mathcal{E}_b$. We take the DF to be

$$f^*(\mathcal{E}^*) = f_b(\mathcal{E})\left[1 + \frac{f_b(\mathcal{E})}{f^*_\infty(\mathcal{E}^*)}\right]^{-1}, \tag{23}$$

which smoothly interpolates between f_b and equation (21). A similar procedure is carried out for the halo and disk.

3. MODELS FOR THE MILKY WAY AND ANDROMEDA GALAXIES

In this section we present models chosen to fit observational data for the Milky Way and Andromeda galaxies. The level of realism in our models is dictated to a large extent by the assumptions upon which they are based. At first glance, the assumption of axisymmetry seems rather restrictive since virtually all disk galaxies exhibit nonaxisymmetric phenomena such as bars and spiral arms. However, our models are subject to nonaxisymmetric instabilities. The program adopted here is to find the best-fit axisymmetric model and determine, through N-body simulations, if the model evolves to a state that more closely matches the actual galaxy. This approach has already been applied to the Milky Way by Sellwood (1985, 1993), Fux (1997), and Valenzuela & Klypin (2003).

Another key assumption is that the model galaxies are comprised of three components, a disk, bulge, and halo, whereas actual disk galaxies also have stellar halos and globular clusters that are typically spheroidal, more extended than the bulge, but (presumably) less extended than the dark halo. It would be straightforward to include such systems in our models, but since they contain relatively little mass, we do not do so here. The inclusion of globular cluster systems might be of interest for studying their evolution during galaxy mergers and interactions.

Along similar lines, the structural parameters of the galactic disks (e.g., radial and vertical scale heights, velocity dispersion tensor) depend on color and metallicity (Dehnen & Binney 1998b), whereas our models assume a single disk component. Stellar disks may, in fact, be more accurately represented as two-component systems with a young thin disk and an old thick disk. Our models can be easily modified to include two or more disklike components, an improvement that may prove relevant for detailed studies of bars and spiral structure.

Our models assume DFs for the bulge and halo that are functions of the energy so that the velocity distribution in these components is necessarily isotropic. By contrast, the velocity distributions in simulated halos are typically biased toward radial orbits with a velocity anisotropy parameter $\beta \equiv 1 - \overline{v_\theta^2}/\overline{v_r^2} \simeq 0.6$ (van den Bosch et al. 1999). Spherical models with nonzero anisotropy parameters can be constructed from functions of E and J, where J is the total angular momentum (Osipkov 1979; Merritt 1985; Baes & Dejonghe 2002). However, J is not an integral of motion of a general axisymmetric system. Moreover, since disks rotate, we can be fairly certain that halos do as well. Thus, realistic halo models require three or more integrals of motion. The velocity structure of dark matter particles will have an effect on the dynamical interaction between the halo and stellar components (e.g., the decay of the bar pattern speed through dynamical friction) and so it may be of interest to consider more general halo DFs. We leave the investigation of these subtle effects for future work.

Perhaps the most severe assumption is that our models include only collisionless components whereas for some disk galaxies a significant fraction of the "disk" mass is locked up in neutral hydrogen gas. Future versions of our models will include H I disks, thereby expanding the applications to models with gas as well as stars.

For each galaxy, we select a set of observational data that are compared with pseudo-observations of the model galaxy to yield a χ^2 statistic. Minimization of χ^2 over the multidimensional parameter space yields the desired best-fit model. In addition, one can include nonobservational constraints so as to select models with certain characteristics (e.g., specific value for the bulge-to-disk mass ratio, baryon fraction, or halo concentration parameter).

In addition to the 15 parameters of Table 1, observer-dependent parameters such as the inclination angle for external galaxies or the galactocentric radius of the Sun for the Milky Way must also be specified. If photometric data are used, then the mass-to-light ratios of the disk and bulge are also required. Depending on the type of observations, some of the parameters may be fixed during the minimization process.

Following Widrow et al. (2003), we employ the downhill simplex algorithm (see, e.g., Press et al. 1986) for the minimization of χ^2. A simplex is a geometrical figure in N dimensions where N is the number of parameters that define the model. During

execution of the algorithm, the simplex moves through parameter space seeking out the minimum of χ^2. As it does so, the simplex changes shape, thus enabling it to move through complicated regions of parameter space. The downhill simplex method has a number of advantages over minimization procedures based on gradients of χ^2 (e.g., the method of steepest descent; see Press et al. 1986 and references therein). In particular, the method appears to be less susceptible to false minima although restarts are always executed to guard against this possibility.

3.1. *The Milky Way*

Numerous authors have attempted to model the Milky Way with early important studies by Bahcall & Soneira (1980) and Caldwell & Ostriker (1981). Bahcall & Soneira (1980) fit star count data together with local values for the scale heights and luminosity functions to parameterize global models of the disk and bulge. Caldwell & Ostriker (1981) considered dynamical constraints (e.g., the Oort constants, rotation curve) in constructing three-component mass models. More recently, Dehnen & Binney (1998a) improved and updated these models by augmenting rotation curve data with dynamical constraints on the vertical structure of the Galaxy in the solar neighborhood.

3.1.1. *Observational Constraints*

The models developed here for the Milky Way are assembled in the same spirit of early mass models but have the advantage that the end result is a fully realized DF for the stars and dark matter of the Galactic system. Seven observational data sets are used to constrain the Milky Way models. Five of these data sets, the inner and outer rotation curves, the Oort constants, the vertical force in the solar neighborhood, and the total mass at large radii, are taken directly from Dehnen & Binney (1998a) and references therein. We also use measurements of the bulge dispersion at a projected distance of 200 pc from the Galactic center (the peak of the dispersion profile) from the compilation of data by Tremaine et al. (2002). Finally, we incorporate estimates of the local velocity ellipsoid from Binney & Merrifield (1998):

1. *Inner rotation curve*.—Observations of H I emission provide a direct measure of the Galactic rotation curve. Inside the solar circle these observations are usually presented in terms of the so-called terminal velocity, $v_{\rm term}$, the peak velocity along a given line of sight at Galactic coordinates $b = 0$ and $|l| < \pi/2$. Assuming that the Galaxy is axisymmetric and the interstellar medium rotates on circular orbits, the H I emission corresponding to $v_{\rm term}$ originates from the galactocentric radius $R = R_0 \sin l$. Relative to the local standard of rest, we have

$$v_{\rm term} = v_c(R) - v_c(R_0) \sin l, \tag{24}$$

where v_c is the circular speed (see, e.g., Binney & Merrifield 1998). Following Dehnen & Binney (1998a), we use data from Malhotra (1995) restricted to the range $\sin l \geq 0.3$ so as to avoid distortions from the bar. In particular, we use values of $v_{\rm term}$ from Figure 7 of her paper at four representative values of $|\sin l|$, averaging the results from the first and fourth quadrants.

2. *Outer rotation curve*.—The radial velocity of an object at Galactic coordinates (l, b) relative to the local standard of rest, $v_{\rm LSR}$, is related to the circular rotation curve through the equation

$$v_{\rm LSR} = \left[\frac{R_0}{R} v_c(R) - v_c(R_0)\right] \cos b \sin l, \tag{25}$$

where $R = (d^2 \cos^2 b + R_0^2 - 2R_0 d \cos b \sin l)^{1/2}$ and d is the distance to the object.

In general, the data consist of a set of measurements ($v_{{\rm LSR},i}$, d_i), which is to be compared with the model estimate $W(R)$ and $d(R)$, where R may be regarded as a free parameter and $W(R) \equiv (R_0/R)v_c(R) - v_c(R_0) \equiv v_{\rm LSR}/\cos b \sin l$. For each data point, we adjust R so as to minimize

$$\chi_i^2 = \left[\frac{W(R) - W_i}{\Delta W_i}\right]^2 + \left[\frac{d(R) - d_i}{\Delta d_i}\right]^2, \tag{26}$$

where $W_i \equiv v_{{\rm LSR},i}/\cos b \sin l$. The χ^2 for this data set is the average of the individual χ_i^2 values.

In what follows we use data from Brand & Blitz (1993) with the same restrictions as in Dehnen & Binney (1998a) (i.e., $l \leq 155^\circ$ or $l \geq 205^\circ$, $d > 1$ kpc, and $W < 0$).

3. *Vertical force above the disk*.—Kuijken & Gilmore (1991) used K dwarf stars as tracers of the gravitational potential above the Galactic plane, thereby placing a constraint on the total mass surface density in the solar neighborhood. They found

$$\frac{|K_z(1.1 \text{ kpc})|}{2\pi G} = 71 \pm 6 \; M_\odot \; \text{pc}^{-2} \tag{27}$$

independent of the relative contributions of the disk and halo. Only by including additional constraints on the local circular speed, galactocentric distance of the Sun, and Oort constants can one ferret out the separate contributions of the disk and halo to the local surface density. Doing so, Kuijken & Gilmore (1991) found

$$\Sigma_{\rm disk} = 48 \pm 9 \; M_\odot \; \text{pc}^{-2}, \tag{28}$$

which is in excellent agreement with estimates of known matter in the solar neighborhood. Since we include constraints on the Oort constants and rotation curve separately, we use equation (27) as a constraint on our models and equation (28) as a consistency check.

4. *Oort constants*.—The Oort constants

$$A \equiv \frac{1}{2}\left(\frac{v_c}{R} - \frac{\partial v_c}{\partial R}\right) \tag{29}$$

and

$$B \equiv -\frac{1}{2}\left(\frac{v_c}{R} + \frac{\partial v_c}{\partial R}\right) \tag{30}$$

measure, respectively, the shear and vorticity in the Galactic disk. Following Dehnen & Binney (1998a), who review the published measurements, we adopt the constraints

$$A = 14.5 \pm 1.5 \text{ km s}^{-1} \text{ kpc}^{-1},$$
$$B = 12.5 \pm 2 \text{ km s}^{-1} \text{ kpc}^{-1}. \tag{31}$$

5. *Local velocity ellipsoid*.—The kinematics of stars in the solar neighborhood provides important constraints on the structure of the Milky Way. The observation that $\overline{v_R^2} \neq \overline{v_z^2}$ already tells us that the disk DF cannot take the form $f = f(E, L_z)$ and necessarily involves a third integral of motion (Binney & Tremaine 1987). Since the KD95 disks are built from three-integral DFs, it is possible to model anisotropic velocity dispersion in Galactic disks. There are two important caveats. The first, already mentioned in the introduction to this section, is that the models assume a single disk component so that the velocity dispersions in the

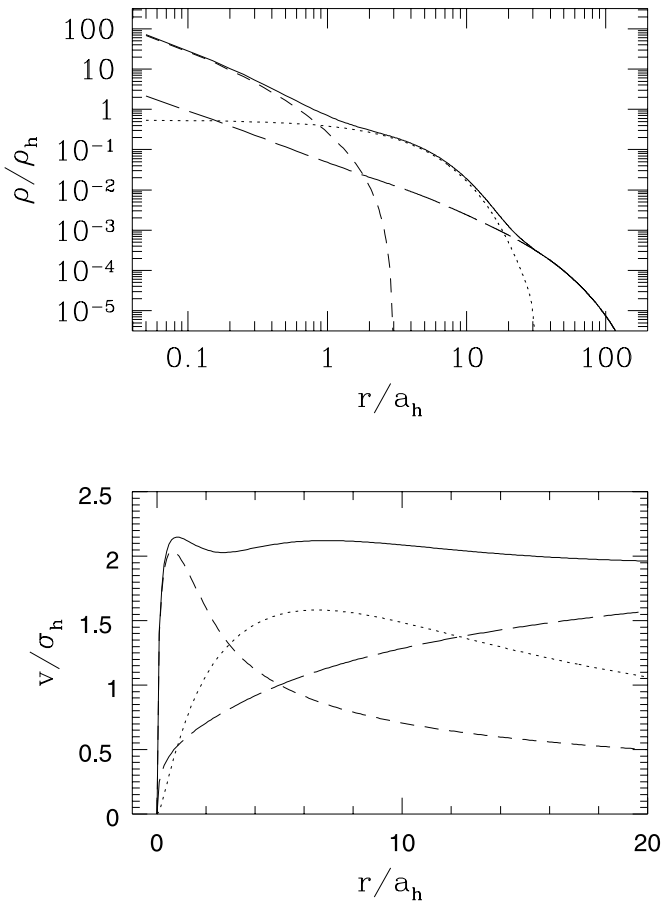

FIG. 3.—Density profile and rotation curve for model MWa. Line types are the same as in Fig. 2.

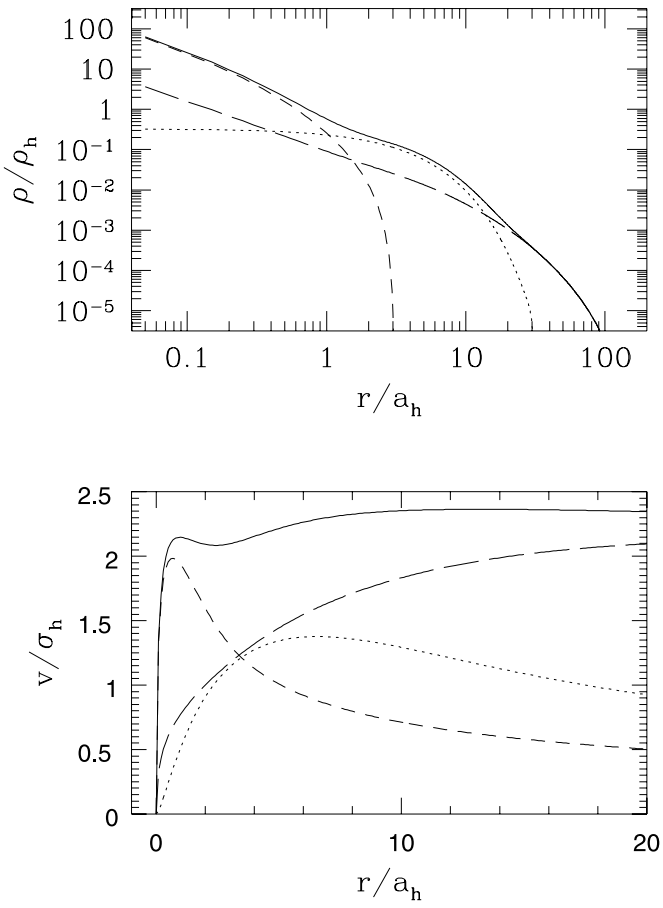

FIG. 4.—Density profile and rotation curve for model MWb.

radial, azimuthal, and vertical directions are single-valued functions of cylindrical radius. In point of fact, the shape of the velocity ellipsoid depends on color (see, e.g., Dehnen & Binney 1998b). Furthermore, the velocity ellipsoid is rotated about the z-axis so that the principle axes do not coincide with the $\hat{R}$- and $\hat{\phi}$-directions. The "vertex deviation" varies from 0° to 30° depending on $B - V$ color.

These limitations can be overcome without too much difficulty (e.g., by including more than one disk component and by generalizing the disk DF to allow for vertex deviation of the velocity ellipsoid). We leave these improvements for future work and consider a single-component disk. For constraints on the velocity ellipsoid, we use values from Table 10.4 of Binney & Merrifield (1998), which were derived from Edvardsson et al. (1993). Binney & Merrifield (1998) give values for the thin and thick disks, and we use a mass-weighted average assuming a 14:1 ratio between these two components (Dehnen & Binney 1998a) with 15% 1 σ error bars.

6. *Bulge dispersion*.—Observations of the LOSVD in the direction of the bulge provide important constraints on the bulge parameters (and, to a lesser extent, the parameters of the other components). Tremaine et al. (2002) have compiled measurements of the LOSVD between 0.085 and 1300 pc. The dispersion profile shows a minimum of $\sim$55 km s^{-1} at $r \simeq 5$ pc and a maximum of 130 km s^{-1} at $r \simeq 200$ pc (see also Kent 1992). The rise of the dispersion profile inside $r \simeq 5$ pc is presumably due to the central black hole, while the detailed shape of the dispersion profile at larger radii may be affected by the barlike shape of the bulge. With this in mind, we average values of the line-of-sight dispersion near the peak to arrive at the single constraint $\sigma_{\rm LOS}(R = 210\ {\rm pc}) = 136 \pm 12$ km s^{-1}.

7. *Mass at large radii*.—The system of satellite galaxies that surround the Milky Way, the Magellanic Stream, and the high-velocity tail of the local stellar velocity distribution provide constraints on the large-scale mass distribution of the Galactic halo. Following Dehnen & Binney (1998a), who base their arguments on work by Kochanek (1996) and Lin et al. (1995), we adopt

$$M(r < 100\ {\rm kpc}) = (7 \pm 2.5) \times 10^{11}\ M_\odot \qquad (32)$$

as a constraint on the mass distribution at large radii.

3.1.2. *Search Strategy*

A χ^2 statistic is calculated by comparing each of the seven data sets described above with pseudo-observations of the model. The pseudo-observations are designed to match closely the actual observations. For example, the LOSVD in the bulge region is found by calculating the velocity dispersion along a given line of sight of bulge "particles" chosen from the DF. In principle, one can add additional layers of realism to the pseudo-observations such as aperture smoothing for LOSVD measurements.

The results are averaged in quadrature to yield a composite χ^2 statistic. In addition to the 15 parameters in Table 1, we must also specify the galactocentric radius of the Sun, R_0. We fix $R_{\rm out}$ and $\delta R_{\rm out}$ to 30 and 1 kpc, respectively. Since the surface density of the disk falls exponentially, varying these values will not affect the model fit. In addition, the rotation parameters of the halo and bulge are fixed so that neither component has net angular momentum. (In principle, incorporating more detailed

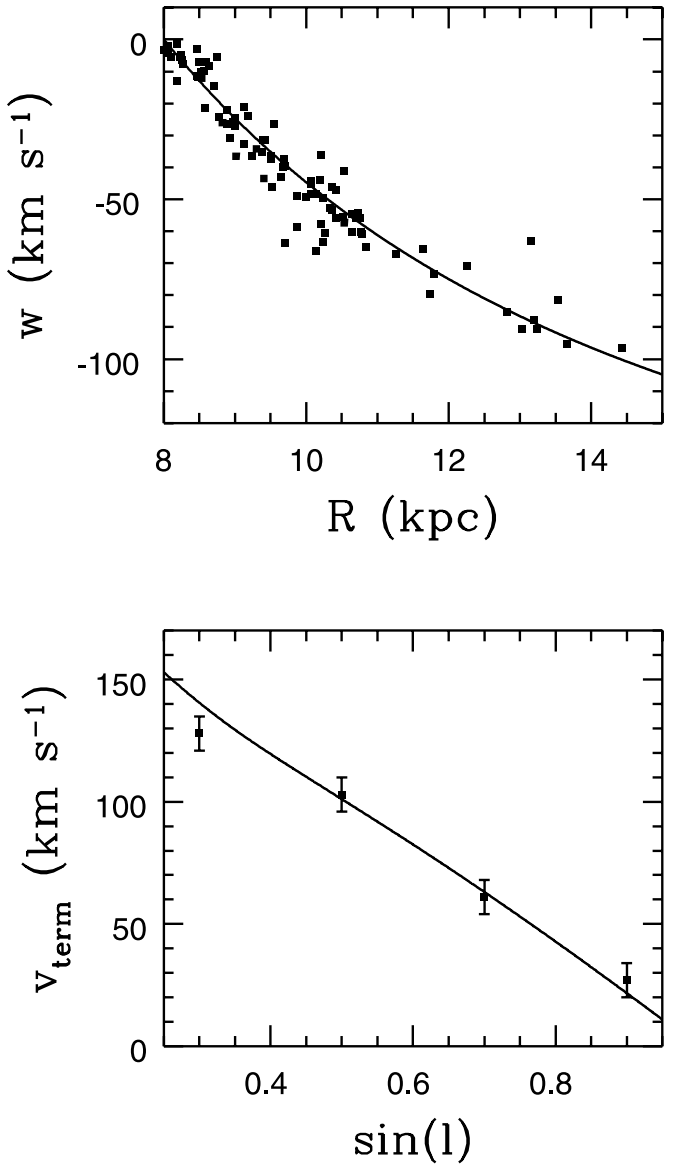

FIG. 5.—Results from the best-fit Milky Way model compared with observations for W (*top*) and $v_{\rm term}$ (*bottom*) as defined in the text.

observations of the bulge would allow us to fit the bulge rotation curve.) We pin the scale length of the radial dispersion profile to half that of the disk scale length (i.e., $R_\sigma = R_d$ so that the σ_R^2 and the surface density have the same exponential decay constant). We also fix $\epsilon_h = 0.2$, which gives a tidal radius larger than 100 kpc. Finally, we run the simplex algorithm with R_0 fixed to different values. In summary, each implementation of the simplex algorithm is run with nine free parameters.

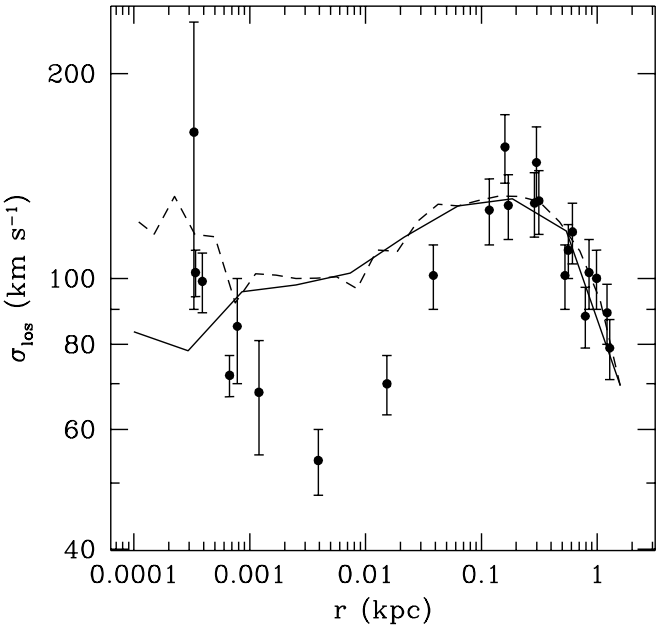

FIG. 6.—Line-of-sight dispersion profile for the bulge region. Data are from a compilation by Tremaine et al. (2002) of published measurements.

3.1.3. *Results*

The parameter set for the best-fit $R_0 = 8$ kpc model (MWa) is given in Table 2. Also given is the parameter set for a Milky Way model with a less massive disk that also has an acceptable χ^2 (MWb). The density profiles and rotation curves for the two models are shown in Figures 3 and 4. We see that the disk dominates the rotation curve in model MWa for 3 kpc $\lesssim R \lesssim$ 12 kpc whereas the disk never dominates the rotation curve of model MWb. We return to this point below.

A comparison of observations of $v_{\rm term}$ and $W(R)$ with model predictions for MWa is shown in Figure 5, while a comparison of observed and predicted quantities for the other observables is given in Table 3. We see that both models provide an excellent fit to the observations.

In Figure 6 we compare the line-of-sight velocity dispersion profile for model MWa with data compiled by Tremaine et al. (2002). Recall that to find the model, a single constraint at 210 pc was used. We see that the agreement between model and observations is excellent for $r > 100$ pc. However, the model dispersion profile at smaller radii is too flat in comparison with the data. The slow rise in the dispersion profile appears to be a feature our models have in common with the η-models of Tremaine et al. (1994) and may point to the necessity for a more complicated DF (e.g., one that depends on two or more integrals of motion).

Figure 6 also includes the dispersion profile obtained for a model that includes a central black hole of mass $3.6\times10^6\ M_\odot$.

TABLE 3
COMPARISON OF OBSERVATIONS AND MODEL PREDICTIONS

Model	χ^2	A	B	$\overline{v_R^2}$	$\overline{\Delta v_\phi^2}$	$\overline{v_z^2}$	$K_z/2\pi G$	$\sigma_{\rm LOS}$ (210 pc)	M (100 kpc)
Observed	...	14.5	−12.5	36	25	20	71	136	70
MWa	0.75	13.6	−12.5	31.7	26.4	19.9	71.7	134	67
MWb	0.91	13.5	−12.9	32.3	27.5	20.0	68.6	134	72

NOTE.—Units are km s^{-1} for the velocity dispersions, $10^{10}\ M_\odot$ for M_b and M(100 kpc), and $M_\odot$ pc^{-2} for $K_z/2\pi G$.

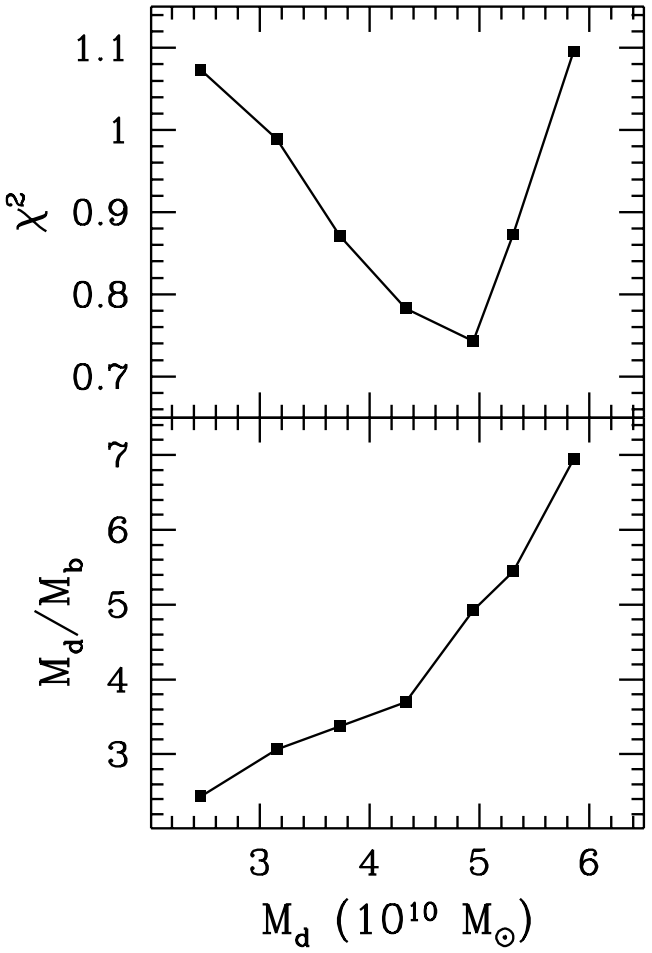

FIG. 7.—The χ^2 statistic as a function of M_d (*top*). The best-fit model is found with M_d fixed. For each case, we show the bulge mass M_b as a function of M_d.

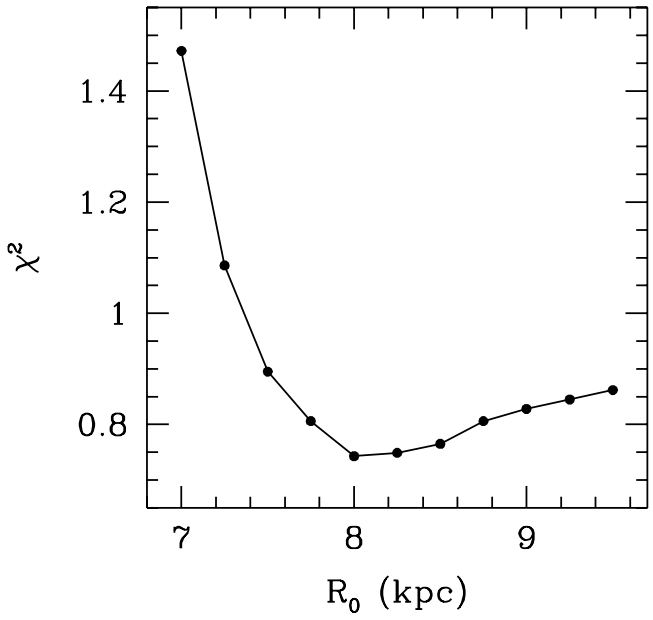

FIG. 8.—The χ^2 statistic as a function of our galactocentric radius, R_0.

This value is roughly twice that found by Tremaine et al. (2002). The agreement between model and observations is poor between 1 and 100 pc perhaps for the aforementioned reasons. However, the model profile does exhibit a minimum at $r \simeq 10$ pc, a feature that is generic to galaxies that are believed to harbor central supermassive objects.

How tightly do the data constrain the model? The answer in part is given in Figures 7 and 8. For Figure 7, M_d is fixed to different values while the remaining eight free parameters are allowed to float. The result is χ^2 as a function of M_d as shown in the top panel. The derived disk-to-bulge mass ratio, again as a function of M_d, is shown in the bottom panel. Evidently, the disk mass can vary by nearly a factor of 2 and still yield an acceptable fit to the data.

A similar analysis for R_0 is shown in Figure 8. Here the minimum in $\chi^2(R_0)$ is fairly flat especially toward larger values of R_0. The preferred value of $R_0 \simeq 8$ kpc agrees with well-known estimates.

For both MWa and MWb, $R_d/R_0 \simeq 0.36$, which is approximately halfway between the two NFW models considered by Dehnen & Binney (1998a; their models 2d and 4d). Table 4 summarizes values for a number of other derived quantities for our models. Column (2) gives the bulge mass. The values for these two models are in excellent agreement with estimates of M_b based on *COBE* DIRBE measurements (Dwek et al. 1995) and gravitational microlensing observations (Bissantz et al. 1997).

Column (3) gives the Toomre Q parameter at $2.5R_d$. Both models have $Q > 1$, indicating that they are stable against local perturbations (Binney & Tremaine 1987). Column (4) gives the local surface density of the disk. Our models evidently bracket the estimates from Kuijken & Gilmore (1991).

Columns (5) and (6) give the total mass and tidal radius for the models. Recall that the tidal radius is controlled by the parameter ϵ_h. We have tuned this parameter so that r_t is roughly equal to the virial radius $R_{\rm vir}$ of the Galaxy as predicted by the standard cosmological model of structure formation. In this scenario, $R_{\rm vir}$ and the mass interior to this radius, $M_{\rm vir}$, are related through the equation

$$M_{\rm vir} = \frac{4\pi}{3}\Delta_{\rm vir}\overline{\rho}R_{\rm vir}^3, \tag{33}$$

where $\overline{\rho}$ is the mean density of the universe and $\Delta_{\rm vir}$ parameterizes the average overdensity of the halo (see Bullock et al. 2001 and references therein). For the currently favored ΛCDM cosmology ($\Omega_\Lambda = 0.3$, $\Omega_m = 0.7$) one finds $\Delta_{\rm vir} = 337$. For both of our Milky Way models, $r_t \simeq 240$ kpc.

Based on these values of r_t, we can estimate the halo concentration parameter $c_{\rm vir} \simeq r_t/a_h$ (col. [7]). Model MWa compensates for the heavy disk by choosing a larger halo scale length, and for this reason its concentration parameter is smaller than that for MWb. Both models have concentration parameters larger than the mean value derived from cosmological simulations but within the 1 σ error bars (Bullock et al. 2001).

TABLE 4

DERIVED QUANTITIES FOR MILKY WAY MODELS

Model (1)	M_b (2)	Q (3)	$K_{z,\rm vis}/2\pi G$ (4)	M_t (5)	r_t (6)	c_t (7)	$\rho(R_0)$ (8)
MWa	1.1	1.3	53	74	239	19	0.0079
MWb	1.2	2.2	39	77	236	27	0.015

NOTES.—Units are kpc for r_t and $M_\odot$ pc^{-3} for $\rho(R_0)$. Otherwise the units are the same as in Table 3.

3.1.4. *Local Dark Matter Density and the Terrestrial Dark Matter Detectors*

Dark matter detection experiments rely on halo models to develop search strategies and to analyze and interpret experimental data. Terrestrial dark matter detectors are sensitive to the local density and velocity-space distribution of dark matter particles. For these experiments, researchers have settled on a standard reference model, namely, Maxwellian velocities with an rms speed of 270 km s^{-1} and a local density of $\rho(R_0) = 0.0079\ M_\odot\ \mathrm{pc}^{-3} \simeq 0.3(\mathrm{GeV}/c^2)\ \mathrm{cm}^{-3}$. This reference model is useful for comparing the sensitivities of different experiments, as well as making contact with predictions from theoretical particle physics.

Our models allow one to study deviations from the standard model while ensuring that observational and dynamical constraints are satisfied. In Figure 9 we compare the local speed distribution for halo particles in models MWa and MWb with that of the standard reference model. The corresponding density is given in column (8) of Table 4. We see that the heavy disk model (MWa) matches up quite well with the standard reference model while the light disk model has a local dark matter density that is a factor of 2 higher. As discussed above, MWa is unstable to bar formation, suggesting a higher value for the local dark matter.

Numerous authors have considered variations on the standard Galactic model such as bulk rotation of the halo, velocity space anisotropy, triaxiality, tidal streams, and small-scale clumpiness. Our models provide a starting point for further investigations along these lines. As described above, rotation may be added to the halo, while velocity-space anisotropy and triaxiality require nontrivial modifications of the DF. In addition, our models are well suited to numerical studies of the tidal disruption of subclumps in the dark halo.

3.2. *Models for M31*

We now take up the challenge of modeling M31, which provides a case study of an external galaxy. The surface brightness profile, the circular rotation curve, and the bulge velocity and dispersion profiles are combined to yield observation-driven models.

Recently, Widrow et al. (2003) combined observations of the types described above to identify a suite of M31 models drawn from the original KD95 set. As one might expect, suitable models were found over a wide range in values for the disk mass-to-light ratio although models with particularly large values were found to be unstable to the formation of a strong bar and could therefore be ruled out.

Our disk-bulge-halo DFs offer the possibility for an improved model of M31. The Hernquist bulge is favored by observations, while the NFW halo is favored by cosmological simulations of structure formation. Moreover, with the new models, the truncation radius of the NFW halo can be varied independently of the inner density profiles of the three components (Fig. 1). Thus, one can tune the truncation radius to correspond to the virial radius as predicted by cosmology or alternatively constrain the outer halo using observations of the M31 satellite system.

3.2.1. *Observations*

Following Kent (1989) and Widrow et al. (2003), we utilize measurements of Andromeda's surface brightness profile, rotation curve, and bulge velocity profiles. We use the global R-band surface brightness profile from Walterbos & Kennicutt (1987), which was obtained by averaging the light distribution over elliptical rings assuming an inclination of 77°.

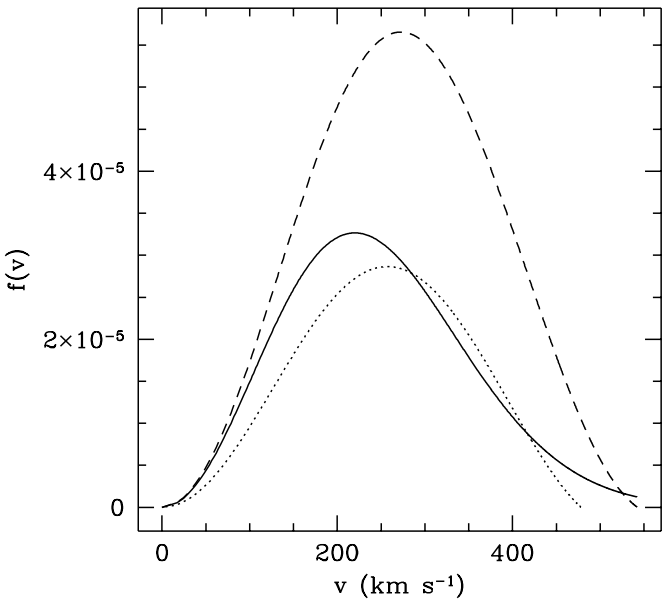

FIG. 9.—Speed distribution of halo particles at the position of the solar system for model M31a (*dotted line*), M31b (*dashed line*), and the standard model used by experimentalists (*solid line*).

The global surface brightness profile represents a small subset of the available photometric data. In principle, a more sophisticated bulge-disk decomposition, where the thickness of the disk and inclination angle enter as free parameters, could be performed using two-dimensional surface brightness maps. However, apparent deviations of the galaxy from axisymmetry suggest that our models cannot adequately reflect this level of detail. For example, the position angle of the major axes of elliptical isophotes varies with galactocentric radius, suggesting that the bulge is barlike and triaxial. Triaxiality can be introduced in a controlled way, for example, by "adiabatically molding" the model into the desired shape (Holley-Bockelmann et al. 2001). Alternatively, one can evolve, via N-body methods, a model galaxy that has a weak bar instability to see if some intermediate state is consistent with the observations (e.g., twisting isophotes). Such an exercise might further constrain the models and help break the mass-to-light degeneracy.

For the rotation curve we combine measurements by Kent (1989) and Braun (1991) using the same kernel smoothing as in Widrow et al. (2003). The composite rotation curve extends from 2 to 25 kpc in galactocentric radii. Although the measurements in Braun (1991) extend to 30 kpc, we ignore data beyond 20 kpc since for this region of the galaxy, measurements were made along a single spiral arm on one side of the galaxy. Stellar rotation and velocity dispersion results from McElroy (1983) are used to constrain the dynamics of the inner 2 kpc of the galaxy. Widrow et al. (2003) attempted to fit the dispersion profiles along the major and minor axes, as well as the bulge rotation profile between 300 and 2000 pc. Acceptable fits were found although, in general, the models had a difficult time simultaneously reproducing a rising rotation curve and falling dispersion profile. One possible explanation is that the "bulge" data are contaminated by the disk (a rapidly rotating, dynamically cold system). Here we use data between 300 and 1000 pc.

The composite χ^2 statistic is given by

$$\chi^2 = \frac{1}{3}\left(\chi^2_{\mathrm{SBP}} + \chi^2_{\mathrm{RC}} + \chi^2_B\right), \tag{34}$$

where $\chi^2_{\rm SBP}$, $\chi^2_{\rm RC}$, and χ^2_B are for the surface brightness profile, rotation curve, and bulge bulk velocity and dispersion profiles, respectively.

3.2.2. *Search Strategy*

Two of the seven parameters that describe the disk DF, the mass and radial scale length, are allowed to vary in the parameter search algorithm. The vertical scale length, truncation radius, and truncation shape parameter are fixed at the values 0.3, 30, and 1 kpc, respectively. Since our data do not depend on the dispersion of disk stars, the parameters σ_{R0} and R_σ are not required for the fitting algorithm although they are required for generating an N-body realization. The halo parameters σ_h and a_h are allowed to vary, while the truncation parameter ϵ_h is fixed to a value large enough so that the truncation radius is well outside the visible part of the galaxy. This parameter is adjusted after a suitable model for the visible part of the galaxy is found. Finally, the four parameters that describe the bulge, a_b, σ_b, f_b, and α_b, are allowed to vary.

3.2.3. *Results*

A wide range of models provide acceptable fits to the observations. Figure 10 is a contour plot of χ^2 in the $(M/L_R)_d$-$(M/L_R)_b$ plane [$(M/L_R)_d$ and $(M/L_R)_b$ are the R-band mass-to-light ratios of the disk and bulge, respectively]. The general structure of a valley running approximately parallel to the $(M/L_R)_d$ axis arises for two reasons. First, the bulge luminosity is constrained by the inner part of the surface brightness profile, while its gravitational potential is constrained by the dispersion data. Hence, $(M/L_R)_b$ is relatively well determined. By contrast, the primary constraint on the disk mass comes from the rotation curve. But since the disk and halo contributions to the rotation curve are similar, one can be played off the other and therefore the $(M/L_R)_d$ is poorly constrained.

The degeneracy with respect to the disk mass-to-light ratio is generic to modeling of spiral galaxies and has been known for some time (see, e.g., van Albada et al. 1985). This degeneracy may be broken by fixing the disk mass-to-light ratio to a theoretically preferred value, e.g., one derived from population synthesis models. Alternatively, one may constrain the disk mass-to-light ratio by requiring that the galaxy model be stable against the formation of a strong bar. As with the Milky Way, M31 may have a weak bar and so absolute stability is not a requirement (or even desirable). However, models with very heavy disks can clearly be ruled out as we demonstrate in the next section. A third possibility is to include an additional data set that probes more directly the disk mass distribution such as disk velocity dispersion measurements as in the study by Bottema et al. (1987) of NGC 5170.

The mass-to-light ratios in Figure 10 must be corrected for foreground and external extinction if we are to make contact with theoretical predictions. Foreground extinction toward M31 is estimated to be 0.41 mag in B (de Vaucouleurs et al. 1976), corresponding to 0.23 mag in R assuming the standard interstellar extinction law (Binney & Merrifield 1998). Estimates of (R band) internal extinction for the disk range from 0.6 (Monnet & Simien 1977) to 0.74 mag (Kent 1989), while formulae in Tully et al. (1998) give 0.64 mag. Assuming 0.65 mag internal extinction for the disk and no internal extinction for the bulge (Kent 1989), $(M/L_R)_d$ and $(M/L_R)_b$ in Figure 10 should be scaled downward by 2.2 and 1.2, respectively, to give χ^2 in terms of intrinsic mass-to-light ratios.

Population synthesis models provide an independent means of constraining the mass-to-light ratios in disk galaxies. Bell & de Jong (2001) provide a table of predicted mass-to-light ratios as a function of various color parameters. In particular, they find

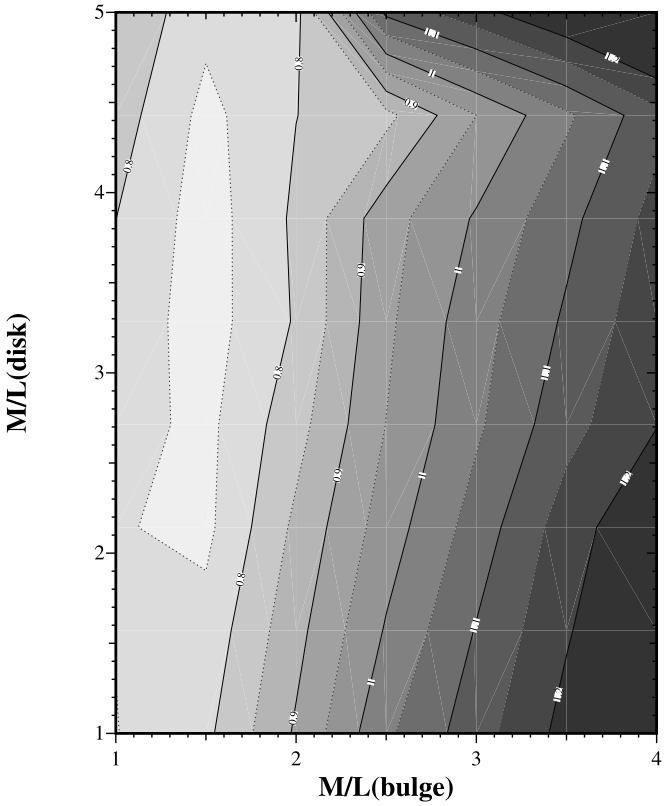

FIG. 10.—Contour plot of χ^2 in the $(M/L_R)_d$-$(M/L_R)_b$ plane.

$$\log_{10}(M/L_R) = -0.820 + 0.851(B - R). \quad (35)$$

For the M31 disk, Walterbos & Kennicutt (1988) find $B - R \simeq 1.53$, which, when corrected for extinction, corresponds to $B - R \simeq 1.18$, implying $(M/L_R)_d \simeq 1.5$ (corrected) or $(M/L_R)_d \simeq 3.4$ (uncorrected). Applying the same formula to the bulge region where $B - R \simeq 1.6$ yields $(M/L_R)_b \simeq 3.2$ (corrected) or 3.9 (uncorrected).

Our results may be compared with those from previous investigations. Kent (1989) modeled the disk and bulge of M31 using rotation curve and bulge dispersion measurements, as well as photometric observations carried out in the r bandpass of the Thuan & Gunn (1976) system. He found (uncorrected) values for the mass-to-light ratios of $(M/L_r)_{\rm disk} = 10.5$ and $(M/L_r)_{\rm bulge} = 5.0$. Using the transformation $r - R = 0.43 + 0.15(B - V)$ from Kent (1985) with a $B - V$ color from Walterbos & Kennicutt (1988), Kent's values become $(M/L_R)_d \simeq 6.2$ and $(M/L_R)_b \simeq 3.0$. Note that Kent (1989) assumes a constant-density halo (i.e., halo with a very large core radius), which explains why his value for $(M/L)_d$ is higher than ours and others (Klypin et al. 2002).

Recent interest in bulge models has been driven in large part by an attempt to understand their connection with galactic supermassive black holes. Magorrian et al. (1998) have constructed dynamical models for bulge–black hole systems in 36 spiral galaxies. For M31, they find a mass-to-light ratio in V band of 4.83 ± 0.1 or $(M/L_R)_b \simeq 3.4$ (uncorrected for extinction).

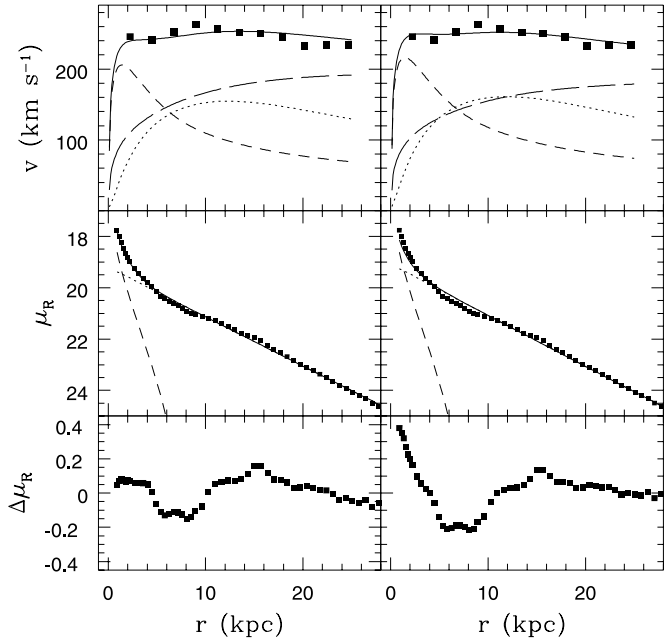

FIG. 11.—Predictions vs. observations for models M31a (*left*) and M31b (*right*). Shown are the rotation curve (*top*), *R*-band surface brightness profile (*middle*), and residuals (predicted – observed) for surface brightness profile (*bottom*). Line types in the rotation curve plots are the same as in previous figures.

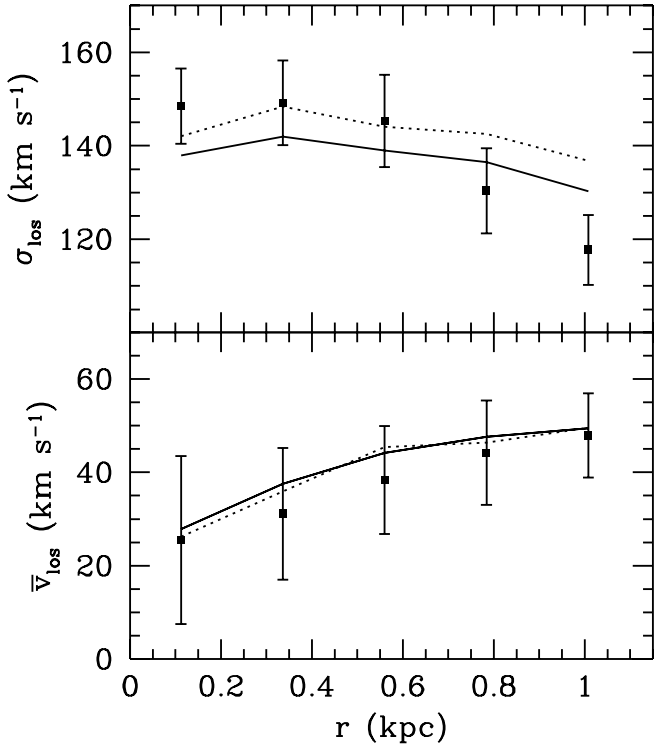

FIG. 12.—Bulge dispersion and bulk rotation profiles for model M31a (*solid line*), M31b (*dotted line*), and observations (*data points*).

To summarize, our analysis alone does little to constrain the disk mass-to-light ratio. As for the bulge, previous modeling and predictions from stellar population studies point to a mass-to-light ratio a factor of 2 higher than our preferred value.

To better understand these results, we consider four models in more detail. Model M31a has disk and bulge mass-to-light ratios set equal to one another and to the value predicted by population synthesis models. This model lies close to the χ^2 valley in Figure 10. The same disk mass-to-light ratio is used in M31b, but here $(M/L_R)_b$ is increased to 3.4 as estimated by Magorrian et al. (1998). The rotation curve and surface brightness profiles for these two models are shown in Figure 11, while the bulge line-of-sight dispersion and bulk velocity profiles are shown in Figure 12. The preference for lower values of $(M/L_R)_b$ is evident in the surface brightness and bulge line-of-sight dispersion profiles. With the higher value of $(M/L_R)_b$, the predicted dispersion profile is too flat, i.e., does not fall fast enough with radius. The simplex algorithm strikes a balance between a bulge that is too dim and one that is too massive but ultimately cannot fit the surface brightness and dispersion profiles as well as the low-$(M/L_R)_b$ model. Note that Kent (1989) has the same difficulty with the bulge dispersion profile while the analysis of Magorrian et al. (1998) is restricted to the innermost 0.′15 (30 pc) of the bulge.

M31c-M31a-M31d form a sequence of models from light to heavy disk mass. The rotation curves for models M31c and M31d are shown in Figure 13.

3.3. *Equilibrium and Stability*

We simulated *N*-body realizations of the four M31 models to test for both the quality of the derived equilibria and stability against bar formation. In all four models, the bulge dominates the innermost part of the rotation curve. In M31c, the disk contribution is subdominant throughout the system, whereas in model M31d, the disk dominates the rotation curve between 5 and 25 kpc. We anticipate that M31d will form a bar while M31c will be stable. For models M31a and M31b the disk contribution to the rotation curve is comparable to that of the other components at about one scale radius.

For each model, we generate an *N*-body realization containing a total of 3.5 million particles (1 million disk particles, 500,000 bulge particles, and 2 million halo particles) and evolve the system using a parallel *N*-body tree code (Dubinski 1996). The extent to which the initial conditions represent a system in equilibrium and its susceptibility to the bar instability are explored by monitoring the surface density of the disk+bulge system, the disk velocity ellipsoid, the disk scale height, and the density profiles of the bulge and halo. We begin by discussing the results for model M31a, which does not form a bar and represents a good test case. The central disk radial velocity dispersion has been set so that the Toomre Q parameter is $Q \approx 1.2$ at $R = 2R_d$. This initial disk is rather cool and is unstable to spiral instabilities arising from the swing amplification of particle shot noise, an effect that leads to emerging spiral structure and disk heating. The disk is also heated through its interactions with halo particles, but this effect is relatively minor with 2 million halo particles and a halo particle mass is only $m_h = 2.9\times10^5\ M_\odot$. (A halo made of $10^6\ M_\odot$ black holes will roughly

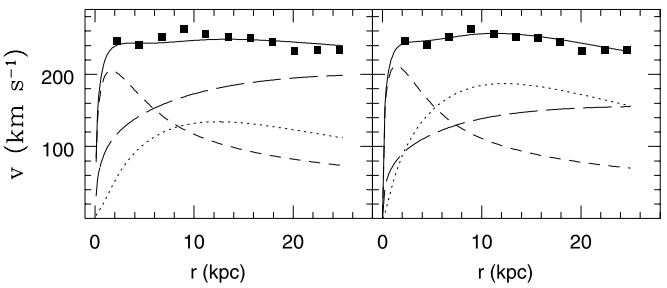

FIG. 13.—Rotation curves for models M31c (*left*) and M31d (*right*).

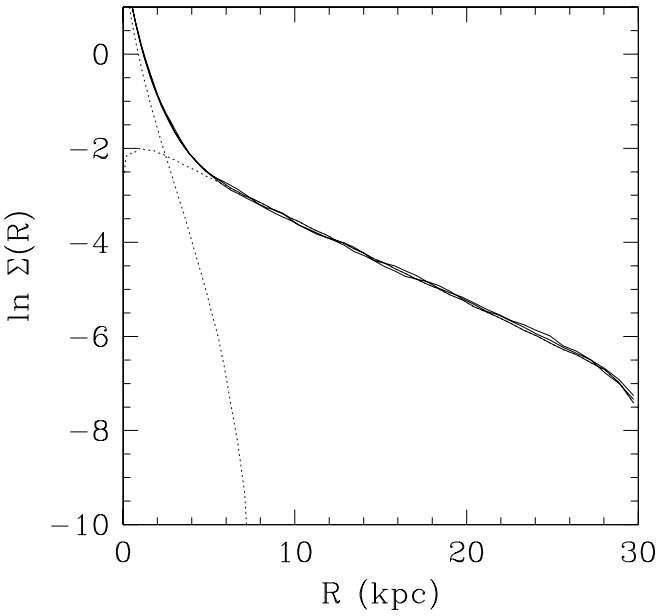

FIG. 14.—Evolution of the surface density profile over 4.8 Gyr. The three solid lines give the total surface density at $t = 0$, 2.4, and 4.8 Gyr. The dotted lines show the separate contributions from the bulge and disk.

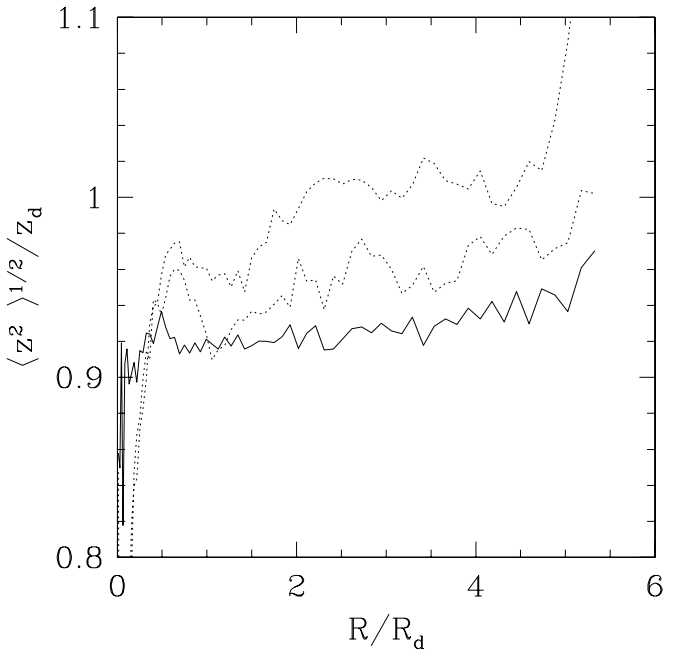

FIG. 16.—Disk scale height evolution at $t = 0$ (*solid line*) and $t = 2.4$ and 4.8 Gyr (*dotted lines*).

double the disk scale height over a Hubble time [e.g., Lacey & Ostriker 1985] and so our halo should have a much smaller effect.)

We ran model M31a for $t = 4.8$ Gyr using 10,000 time steps. The particle softening radius was set to $s = 50$ pc so the number of time steps was more than adequate to follow orbits down to the softening radius in the galaxy core. The first impression is that the initial conditions are almost in perfect equilibrium with essentially no transient readjustment of the disk at start-up, i.e., no evidence of the imperfections in the initial conditions that are present in other methods (e.g., Hernquist 1993). Figure 14 shows the disk+bulge surface density profile at $t = 0$, 2.4, and 4.8 Gyr along with the disk and bulge initial profiles. There is no change in the profile over the 4.8 Gyr integration and there is no sign of a bar. Figure 15 shows the evolution of the radially averaged disk velocity ellipsoid throughout the disk and reveals the effect of natural heating through the growth of spiral structure. The disk velocity ellipsoid at $R = 15$ kpc (about 3 disk exponential scale lengths) changes from $(\sigma_R,\ \sigma_\phi,\ \sigma_z) = (22, 15, 18)$ to (31, 22, 19) km s^{-1} after 4.8 Gyr. Another indicator of disk evolution and heating is the vertical scale height. Figure 16 shows the variance in disk particle height above the midplane as an estimator of disk scale height at three times. There is some evolution with the scale height growing by about 10%, showing the good quality and relatively low shot-noise effect in the models. The apparent flaring beyond about $R = 4R_d$ may result partially from poor vertical force resolution due to discrete sampling of the disk. Since we choose a constant disk particle mass, the particle number density drops off quickly at large radii.

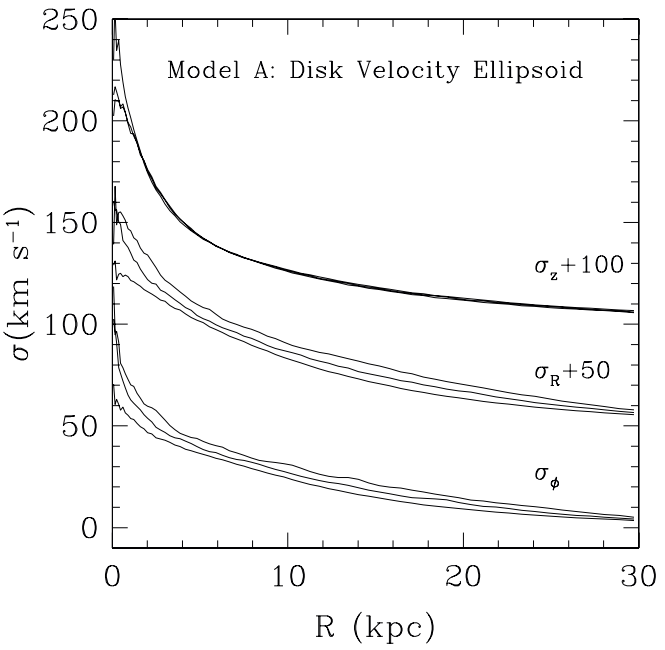

FIG. 15.—Evolution of the disk velocity ellipsoid over 10 Gyr. The profiles of the velocity dispersions are shown at $t = 0.0$, 2.4, and 4.8 Gyr, showing a slow increase over the disk.

Figure 17 shows the density profile of the bulge and halo over the course of the simulation. The denser bulge develops a core radius of $r_c \approx 300$ kpc because of the use of force softening while the halo maintains its r^{-1} cusp. We see below in models with black holes that the cusp profile can be maintained if smaller softening lengths and smaller time steps are used. We also examined the evolution of the halo shape profile as a further test. Near the vicinity of the disk, the halo profile shape is flattened by the presence of the disk potential and so that flattening should remain unchanged if the system is in proper equilibrium. We compute the shape of the best-fit ellipsoidal density contours as a function of radius at the start and end of the simulation using the normalized inertial tensor using the method described in Dubinski & Carlberg (1991) (Fig. 18). This shows that the halo is flattened into an oblate spheroid with $q \simeq 0.8$ near the disk and then becomes spherical at larger radii. With the exception of the central point where softening effects modify profiles, the shape profile remains unchanged

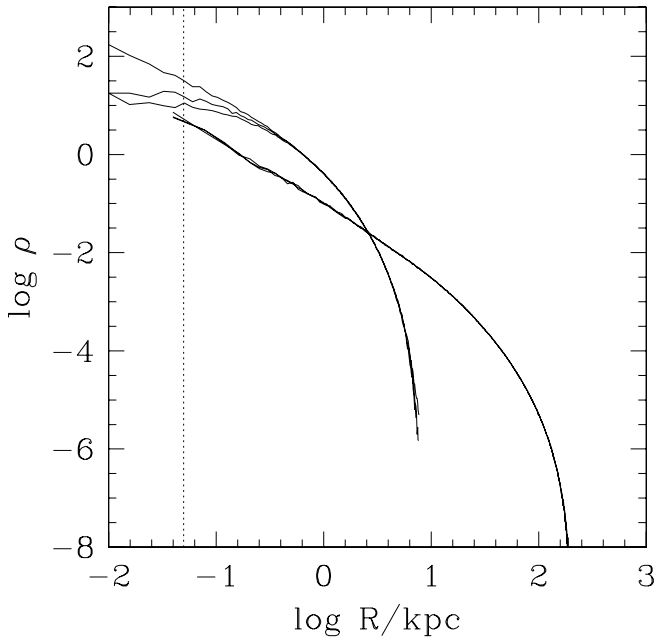

FIG. 17.—Bulge and halo radial density profiles over 4.8 Gyr. The vertical dotted line corresponds to the softening length. A constant-density core develops in the bulge on the scale of the softening length of $s = 50$ pc.

throughout the simulation, implying a good choice of equilibrium. In summary, the method produces an excellent equilibrium configuration of a spiral galaxy. The gradual heating of the disk can be attributed to the formation of transient spiral structure and to a lesser extent heating by halo particles.

Simulations of the remaining models also show clean initial equilibria. Only model M31d develops a bar. The bar forms at 3 Gyr and persists until the end of the simulation at $t = 4.8$ Gyr. At the end of the simulation the bar has a length of $r_b = 7.7$ kpc with a pattern speed of 23 km s^{-1} kpc^{-1} and a corotation radius of $D_L = 9.8$ kpc. The ratio $D_L : r_b = 1.3$ makes this a "fast" bar in the standard nomenclature (e.g., O'Neill & Dubinski 2003) at least at this stage of the simulation. While M31 appears to have a triaxial barlike bulge, at present, it does not appear to be a well-developed barred spiral. The absence of a bar in M31 suggests that the disk mass in model M31d is too great and that one of the other models is more acceptable for M31.

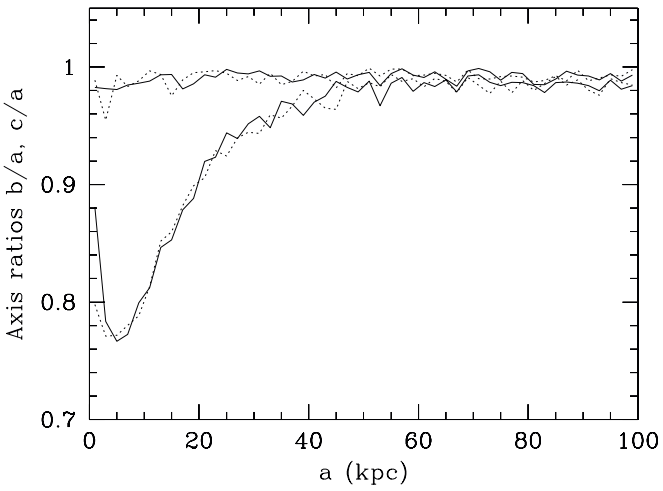

FIG. 18.—Halo axis ratio profile at the start (*solid line*) and end (*dashed line*) of the simulation over 4.8 Gyr. With the exception of the central point, the axis ratio of the halo remains essentially constant throughout the simulation.

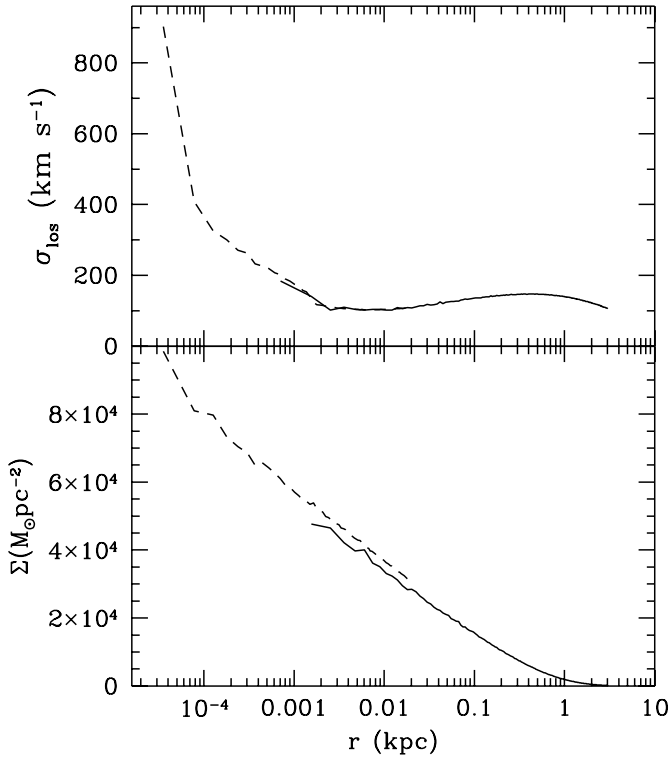

FIG. 19.—Velocity dispersion (*top*) and surface brightness (*bottom*) profiles in the bulge.

We also simulated the two Milky Way models and found little evolution in the velocity ellipsoid, vertical scale height, surface density, and space density, again illustrating the excellent quality of the models as a means of setting up initial conditions for *N*-body simulations. Not surprisingly, model MWa (where the disk provides the dominant contribution to the rotation curve at intermediate radii) develops a bar while MWb appears to be stable.

3.4. *Incorporating a Black Hole*

In this section we examine an axisymmetric model of M31 augmented by a central black hole. M31 is the nearest galaxy with a demonstrable central black hole but unfortunately exhibits a complex central structure in the form of a double nucleus (Lauer et al. 1993; Bacon et al. 1994). Estimates of the black hole mass based on dynamical models and the observed bulge surface brightness and velocity dispersion profiles fall in the range $(3-8.5)\times10^7\ M_\odot$ (Tremaine 1995; Kormendy & Bender 1999; Bacon et al. 2001).

As an illustration of our models, we place a black hole of mass $3\times10^7\ M_\odot$ at the center of model M31a. Figures 19 and 20 show the line-of-sight velocity dispersion and surface density profiles. To generate the inner portion of the curves (*dashed lines*) in Figure 19, we sample 10 million particles from the bulge DF within a thin tube 20 pc in radius centered on the galaxy and aligned with the symmetry axis. The dispersion profile exhibits the characteristic intermediate minimum and maximum seen in the data (Tremaine 1995).

We also simulate a galaxy model including a black hole to test the quality of the equilibrium focusing on the nuclear region close to the black hole. The black hole moves freely as a single particle within the simulation. For this test, we put most of the particles in the bulge, $N = 10^7$, so the ratio of the black hole mass to the bulge particle mass is $\sim10^4$. The enclosed mass of

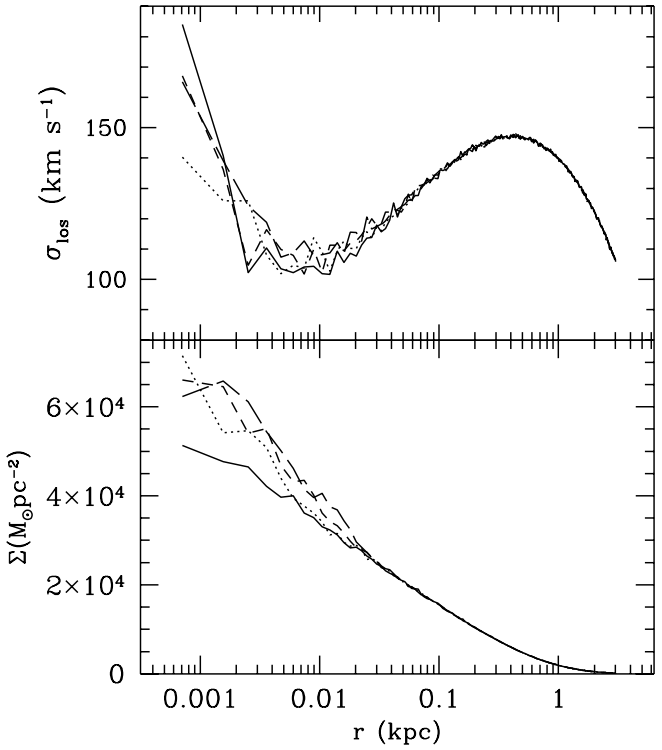

FIG. 20.—Evolution of the velocity dispersion and surface brightness profiles around the central black hole. *Solid line*: $t = 0$; *dotted line*: $t \simeq 10^5$ yr; *short-dashed line*: $t \simeq 2\times10^5$ yr; *long-dashed line*: $t \simeq 3\times10^5$ yr. The orbital time for the black hole at 1 pc is 1.7×10^4 yr.

bulge stars equals the black hole mass at a radius $r = 34$ pc. The halo and disk are represented by 2 million and 1 million particles, respectively, but their particles are unlikely to interact with the black hole in this test. We set the particle and black hole softening length to $s = 1$ pc and use a single time step of $\Delta t = 100$ yr. Even with a total of $N = 10^7$ particles in the bulge, there are only 13 bulge particles initially within the softening radius. Figure 20 also shows the evolution of the model, focusing on the central region surrounding the black hole. The simulation is run for 3000 time steps, corresponding to approximately 18 orbital times at a radius of 1 pc. We see that there is some evolution of the system; toward the center, the velocity dispersion fluctuates slightly within $r \sim 10$ pc and the surface density increases slightly. At $r = 1$ pc where there are only a dozen or so particles, we expect larger initial variations that may explain the settling to a slightly higher density. Nevertheless, the profiles remain close to the initial state, suggesting that the equilibrium is reasonable. These effects may also result indirectly from using force softening or may be a reflection of the approximations that have gone into the DF. Clearly, high numerical resolution is needed to treat the dynamics of stars around a central black hole, and the short orbital times make these technically difficult and costly.

Models such as this one may be used as initial conditions for numerical experiments of black hole dynamics during galaxy merger events such as the simulations by Milosavljević & Merritt (2003) and will be explored in future investigations.

4. SUMMARY AND DISCUSSION

Our goals in this paper have been threefold. First, we have presented a new set of model DFs for multicomponent disk galaxies. Second, we have identified particular models that fit observational data for the Milky Way and M31. Finally, we have explored the stability of the models using numerical simulations.

Our DFs represent self-consistent axisymmetric equilibrium solutions to the Poisson and CB equations. The disk and bulge DFs are motivated by observations, while the halo DF is motivated by results from cosmological *N*-body simulations. The models permit the inclusion of a central supermassive black hole.

Historically, two approaches have been used to construct DFs for equilibrium systems (Binney & Tremaine 1987). The first approach is to propose a DF built from chosen functions of the integrals of motion and then calculate the density by solving the Poisson equation. The second is to calculate the DF from the desired density profile via an integral equation known as the Abel transform. Our DFs are the product of a hybrid scheme. The DF for the isolated NFW halo was derived from the Abel transform, modified by the energy mapping as described in the text, and then used for the halo in the composite system.

Our models are defined by 15 free parameters, which may be tuned to fit a wide range of observational data. Typically most of the parameters are poorly constrained. A galaxy's surface brightness profile is, in general, adequate to fix the disk scale length and, in combination with velocity dispersion and rotation curve measurements, provides a constraint on the disk mass and halo and bulge structural parameters. However, degeneracies remain primarily due to uncertainties in the disk and bulge mass-to-light ratios. Theoretical considerations such as results from population synthesis studies or numerical experiments of the bar instability can help narrow down the field of acceptable models. Additional data for external galaxies such as velocity dispersion measurements in the disk may help break the M/L degeneracy. Observations of edge-on spiral galaxies can be used to constrain the vertical scale height and disk truncation parameters (Kregel et al. 2002).

We have constructed sequences of models for the Milky Way and M31 that provide excellent fits to available data. The models serve to illustrate the general procedure for searching a large parameter space to find acceptable models for particular galaxies.

A primary purpose of our models is to provide initial conditions for *N*-body experiments, and well-developed techniques allow one to sample the DFs with arbitrary numbers of particles. Through a series of numerical experiments, we have explored the quality of the models as initial conditions and their stability to the formation of bars. Models in which the disk contribution to the rotation curve is always subdominant to that of the bulge and halo tend to be stable against bar formation and therefore provide the best laboratory to study the quality of the model DFs. Our analysis of one such model indicates that the DFs do indeed provide excellent initial conditions. The radial profiles of the space density, surface density, velocity dispersion tensor, and vertical scale height all remain relatively constant over 4.8 Gyr. Areas where we do see some evolution may be understood from simple considerations. For example, the bulge evolves from Hernquist cusp to core inside the softening length because the velocity distribution is calculated assuming an unsoftened force law. Spiral density waves, generated by swing amplification of shot noise, cause the disk to thicken, but only by about 10%.

Models in which the disk contribution to the rotation curve is dominant over some range in radius develop strong bars. We confirm this well-known result for both Milky Way and M31 models.

Our models allow for the addition of a central supermassive black hole. Our prescription for doing this maintains the density

distribution of the black hole–less models while modifying the velocities to establish a new dynamical equilibrium near the black hole. The velocity dispersion profiles of our black hole models have the right characteristics to match the data, namely, high dispersion near the black hole falling to a minimum at tens of parsecs, rising at a radius of a hundred or so parsecs, and then falling again as one moves farther out in radius. Thus, we may be able to model galaxies from the sphere of influence of the black hole out to the virial radius, an impressive dynamic range of 5 or more orders of magnitude.

There are numerous open avenues for future work. The model fitting algorithm can accommodate any number and type of observations, and one may add to the pseudo-observations layers of realism such as statistical fluctuations and the effects of seeing. Our M31 study used a small subset of the available photometric and kinematic data. Two-dimensional surface brightness and dispersion maps reveal the presence of the bar and may be compared with corresponding maps from the "evolved" models, providing a further constraint on the model.

A classic problem in galactic dynamics is the disruption of satellite systems by the tidal field of the parent galaxy. The discovery of an arc of stars associated with the Sagittarius dwarf galaxy (see Majewski et al. 2003 and references therein) has intensified interest in performing simulations of the tidal disruption of this system (Ibata et al. 1997; Helmi 2004; see also Geehan et al. 2005 for a study of the Andromeda stream in a disk-bulge-halo model of M31). Our models offer the possibility of performing such simulations of realistic and fully self-consistent models for both parent and satellite systems. Since a primary goal of previous investigations has been to constrain the shape of the Galactic halo, our models will have to be extended to include triaxial systems if they are to be useful in this endeavor. The extension to triaxial systems might be accomplished by adiabatically molding the models as in Holley-Bockelmann et al. (2001).

Our models might be extended in other important ways such as the inclusion of a globular cluster system or thick disk as discussed in the text. Perhaps the most significant and challenging improvement would be to add a gas component and star formation since this would enable the study of spiral structure and bar formation with a far greater level of realism.

It is a pleasure to thank S. Courteau, R. Henriksen, K. Perrett, and S. Kazantzidis for useful conversations. This work was supported, in part, by the Natural Science and Engineering Research Council of Canada and the Canadian Foundation for Innovation.

REFERENCES

Bacon, R., Emsellem, E., Combes, F., Copin, Y., Monnet, G., & Martin, P. 2001, A&A, 371, 409
Bacon, R., Emsellem, E., Monnet, G., & Nieto, J. L. 1994, A&A, 281, 691
Baes, M., & Dejonghe, H. 2002, A&A, 393, 485
Bahcall, J. N., & Soneira, R. M. 1980, ApJS, 44, 73
Barnes, J. 1988, ApJ, 331, 699
Bell, E. F., & de Jong, R. S. 2001, ApJ, 550, 212
Binney, J. 1987, in The Galaxy, ed. G. Gilmore & B. Carswell (Dordrecht: Reidel), 399
Binney, J., & Merrifield, M. 1998, Galactic Astronomy (Princeton: Princeton Univ. Press)
Binney, J., & Tremaine, S. 1987, Galactic Dynamics (Princeton: Princeton Univ. Press)
Bissantz, N., Englmaier, P., Binney, J., & Gerhard, O. 1997, MNRAS, 289, 651
Blumenthal, G. R., Faber, S. M., Flores, R., & Primack, J. R. 1986, ApJ, 301, 27
Bottema, R. 1993, A&A, 275, 16
Bottema, R., van der Kruit, P. C., & Freeman, K. C. 1987, A&A, 178, 77
Brand, J., & Blitz, L. 1993, A&A, 275, 67
Braun, R. 1991, ApJ, 372, 54
Bullock, J. S., Kolatt, T. S., Sigad, Y., Somerville, R. S., Kravtsov, A. V., Klypin, A. A., Primack, J. R., & Dekel, A. 2001, MNRAS, 321, 559
Caldwell, J. A. R., & Ostriker, J. P. 1981, ApJ, 251, 61
Clutton-Brock, M., Innanen, K. A., & Papp, K. A. 1977, Ap&SS, 47, 299
Courteau, S., de Jong, R. S., & Broeils, A. H. 1996, ApJ, 457, L73
Debattista, V. P., & Sellwood, J. A. 1998, ApJ, 493, L5
———. 2000, ApJ, 543, 704
Dehnen, W. 1993, MNRAS, 265, 250
Dehnen, W., & Binney, J. 1998a, MNRAS, 294, 429
———. 1998b, MNRAS, 298, 387
———. 1996, NewA, 1, 133
———. 1998, ApJ, 502, 141
de Vaucouleurs, G. 1948, Ann. d'Astrophys., 11, 247
de Vaucouleurs, G., de Vaucouleurs, A., & Corwin, H. G. 1976, Second Reference Catalog of Bright Galaxies (Austin: Univ. Texas Press)
Dubinski, J., & Carlberg, R. G. 1991, ApJ, 378, 496
Dubinski, J., & Kuijken, K. 1995, ApJ, 442, 492
Dubinski, J., Mihos, C., & Hernquist, L. 1999, ApJ, 526, 607
Dwek, E., et al. 1995, ApJ, 445, 716
Edvardsson, B., Anderson, J., Gustafsson, B., Lambert, D. L., Nissen, P. E., & Tomkin, J. 1993, A&A, 275, 101
Evans, N. W., & Wilkinson, M. I. 2000, MNRAS, 316, 929
Flores, R., Primack, J. R., Blumenthal, G. R., & Faber, S. M. 1993, ApJ, 412, 443
Fux, R. 1997, A&A, 327, 983
Garcia-Ruiz, I., Kuijken, K., & Dubinski, J. 2002, MNRAS, 337, 459
Geehan, J. J., Fardal, M. A., Babul, A., & Guhathakurta, P. 2005, MNRAS, submitted (astro-ph/0501240)
Helmi, A. 2004, ApJ, 610, L97
Hernquist, L. 1990, ApJ, 356, 359
———. 1993, ApJS, 86, 389
Holley-Bockelmann, K., Hihos, J. C., Sigurdsson, S., & Hernquist, L. 2001, ApJ, 549, 862
Ibata, R., Wyse, R. F. G., Gilmore, G., Irwin, M. J., & Suntzeff, N. B. 1997, AJ, 113, 634
Innanen, K. A. 1973, Ap&SS, 22, 393
Kazantzidis, S., Magorrian, J., & Moore, B. 2004, ApJ, 601, 37
Kent, S. 1985, ApJS, 59, 115
———. 1989, AJ, 97, 1614
———. 1992, ApJ, 387, 181
King, I. R. 1966, AJ, 71, 64
Klypin, A., Zhao, H., & Sommerville, R. S. 2002, ApJ, 573, 597
Kochanek, C. S. 1996, ApJ, 457, 228
Kormendy, J., & Bender, R. 1999, ApJ, 522, 772
Kregel, M., van der Kruit, P. C., & de Grijs, R. 2002, MNRAS, 334, 646
———. 1995, MNRAS, 277, 1341 (KD95)
Kuijken, K., & Gilmore, G. 1991, ApJ, 367, L9
Lacey, C. G., & Ostriker, J. P. 1985, ApJ, 299, 633
Lauer, T. R., et al. 1993, AJ, 106, 1436
Lin, D. N. C., Jones, B. F., & Klemola, A. R. 1995, ApJ, 439, 652
Lokas, E. L., & Mamon, G. A. 2001, MNRAS, 321, 155
Magorrian, J., et al. 1998, AJ, 115, 2285
Majewski, S. R., et al. 2003, ApJ, 599, 1082
Malhotra, S. 1995, ApJ, 448, 138
McElroy, D. B. 1983, ApJ, 270, 485
Merritt, D. 1985, AJ, 90, 1027
Milosavljević, M., & Merritt, D. 2003, ApJ, 596, 860
Mo, H. J., Mao, S., & White, S. D. M. 1998, MNRAS, 295, 319
Monnet, G., & Simien, F. 1977, A&A, 56, 173
Moore, B., Kazantzidis, S., Diemand, J., & Stadel, J. 2004, MNRAS, 354, 522
Navarro, J. F., Frenk, C. S., & White, S. D. M. 1996, ApJ, 462, 563
O'Neill, J. K., & Dubinski, J. 2003, MNRAS, 346, 251
Osipkov, L. P. 1979, Soviet Astron. Lett., 5, 49
Perez, J., & Aly, J.-J. 1996, MNRAS, 280, 689
Press, W. H., Flannery, B. P., Teukolksy, S. A., & Vettelring, W. T. 1986, Numerical Recipes (Cambridge: Cambridge Univ. Press)
Rohlfs, K., & Kreitschmann, J. 1988, A&A, 201, 51
Sellwood, J. A. 1985, MNRAS, 217, 127
———. 1993, in AIP Conf. Proc. 278, Back to the Galaxy, ed. S. S. Holt & F. Verter (New York: AIP), 133

Shu, F. H. 1969, ApJ, 158, 505
Simien, F., & de Vaucouleurs, G. 1986, ApJ, 302, 564
Thuan, T. X., & Gunn, J. E. 1976, PASP, 88, 543
Tremaine, S. 1995, AJ, 110, 628
Tremaine, S., Richstone, D. O., Byun, Y.-I., Dressler, A., Faber, S. M., Grillmair, C., Kormendy, J., & Lauer, T. R. 1994, AJ, 107, 634
Tremaine, S., et al. 2002, ApJ, 574, 740
Tully, R. B., Pierce, M. J., Huang, J.-S., Saunders, W., Verheijen, M. A. W., & Witchalls, P. L. 1998, AJ, 115, 2264
Valenzuela, O., & Klypin, A. 2003, MNRAS, 345, 406
van Albada, T. S., Bachall, J. N., Begeman, K., & Sancisi, R. 1985, ApJ, 295, 305
van den Bosch, F. C., Lewis, G. F., Lake, G., & Stadel, J. 1999, ApJ, 515, 50
Walterbos, R. A. M., & Kennicutt, R. C., Jr. 1987, A&AS, 69, 311
———. 1988, A&A, 198, 61
Widrow, L. M. 2000, ApJS, 131, 39
Widrow, L. M., Perrett, K. M., & Suyu, S. H. 2003, ApJ, 588, 311
Wilkinson, M. I., & Evans, N. W. 1999, MNRAS, 310, 645
Young, P. 1980, ApJ, 242, 1232
Zhao, H. 1997, MNRAS, 287, 525